Enabling Higher Order Lamb Wave Acoustic Devices With Complementarily Oriented Piezoelectric Thin Films

Ruochen Lu, *Member, IEEE*, Yansong Yang, *Member, IEEE*, Steffen Link, *Student Member, IEEE*,
and Songbin Gong, *Senior Member, IEEE*

Abstract—In this work, we present a new paradigm for enabling gigahertz higher-order Lamb wave acoustic devices using complementarily oriented piezoelectric (COP) thin films. Acoustic characteristics are first theoretically explored with COP lithium niobate (LiNbO$_3$) thin films, showing their excellent frequency scalability, low loss, and high electromechanical coupling (k^2). Acoustic resonators and delay lines are then designed and implemented, targeting efficient excitation of higher-order Lamb waves with record-breaking low loss. The fabricated resonator shows a 2nd-order symmetric (S2) resonance at 3.05 GHz with a high quality factor (Q) of 657, and a large k^2 of 21.5% and a 6th-order symmetric (S6) resonance at 9.05 GHz with a high Q of 636 and a k^2 of 3.71%, both among the highest demonstrated for higher-order Lamb wave devices. The delay lines show an average insertion loss (IL) of 7.5 dB and the lowest reported propagation loss of 0.014 dB/μm at 4.4 GHz for S2. Notable acoustic passbands up to 15.1 GHz are identified. Upon further optimizations, the proposed COP platform can lead to gigahertz low-loss wideband acoustic components.   [2020-0127]

Index Terms—5G new radio, acoustic resonators, acoustic delay lines, lamb wave, lithium niobate, piezoelectric devices, RF microsystems, thin-film devices.

I. INTRODUCTION

THE emerging fifth-generation (5G) New Radio (NR) has sparked the recent development of various radio frequency (RF) signal processing functions [1]. More specifically, enhanced mobile broadband (eMBB), as one critical 5G application, aims to communicate at higher center frequencies with broader bandwidth than the current fourth-generation (4G) wireless communication [2]. With the Third Generation Partnership Project (3GPP) releasing the first group of frequency band specifications for 5G NR [3], the RF spectrum between 3 and 6 GHz is believed to be the primary venue for the initial 5G eMBB deployment. This frequency range provides a well-balanced availability of large bandwidths and low free path loss, and it is considered compatible with the current RF

front-end architecture [3]. Therefore, the key to implementing the envisioned 5G NR at sub-6 GHz lies in the development of the essential RF signal processing components, e.g., acoustic filters, to accommodate the requirements of 5G NR [4], [5].

One proposed path for 5G RF acoustic devices is to scale down the critical dimensions directly (e.g., film thickness and electrode feature size) of the conventional RF acoustic platforms, such as surface acoustic wave (SAW) [6]–[8], and film bulk acoustic resonators (FBAR) [9]–[11], to operate at the sub-6 GHz bands. However, three significant challenges prohibit such an approach to meet the 5G NR requirements. First, the incumbent piezoelectric platforms cannot provide adequate fractional bandwidth (FBW) due to the limited effective electromechanical coupling (k^2) [12]. Second, merely reducing the dimensions of conventional acoustic devices inevitably results in increased insertion loss (IL) at higher frequencies [13], [14], due to the exacerbated material damping, electrical loading, and the more pronounced surface losses [15]–[17]. Third, scaling down devices (e.g., film thickness, electrode width) for attaining a higher center frequency and matching the system impedance might lead to worsened power handling and increased nonlinearity because more acoustic energy is concentrated in a smaller volume [18]–[20]. To address the challenges, novel acoustic platforms have been investigated in the past few years, including transferred thin films on costly substrates [21]–[25], new materials and acoustic modes with larger piezoelectric coefficients [26]–[33], and incorporated additional lumped electromagnetic (EM) elements [34]–[37].

Among various emerging acoustic solutions, first-order antisymmetric (A1) Lamb wave devices in single-crystal Z-cut lithium niobate (LiNbO$_3$) thin films have been demonstrated with low loss, wide bandwidth, and large feature sizes. The promising performance arises from the simultaneously achieved k^2 as high as 30%, low damping, and fast phase velocity across the sub-6 GHz NR bands [38]–[41]. Fundamentally, the large piezoelectric coefficient d_{15} [42], low acoustic loss, and EM loss tangent [15], [43] are the reasons for these advances. Leveraging the A1 mode in LiNbO$_3$, both the resonant – e.g., resonators and filters [44]–[46] – and the non-resonant – e.g., acoustic delay lines (ADLs) [47] – have been reported with record-breaking IL and FBW. However, several bottlenecks emerge for further improving A1 prototypes as the film thickness reduces to less than 600 nm

LiNbO$_3$ for operation beyond 3 GHz. The thinner film leads to more severe surface losses [16], thus limiting the quality factor (Q) of the demonstrated A1 resonators (below 400 [38]–[40]), and the propagation loss (PL) of A1 ADLs (above 0.02 dB/μm [47]). Moreover, lateral field excited A1 devices with spurious mode suppression have a small capacitance per unit area [48]. Consequently, it results in a relatively large footprint [44]–[46]. Third, the suspended thin-film bears severe thermally induced nonlinearity because of the limited thermal conductance to surroundings [18], [19]. To address these issues, one alternative for operating at 5G NR bands with a thicker LiNbO$_3$ thin film is to excite the higher-order Lamb waves [49]–[51]. Unfortunately, k^2 of Lamb modes diminish at a higher mode order when excited with the top-electrode-only topology due to the partial cancellation of the generated charge in the thickness direction [50]. Therefore, advancing thin-film LiNbO$_3$ based acoustic devices calls for a new paradigm for enabling gigahertz higher-order Lamb modes.

This work presents complementarily oriented piezoelectric (COP) thin films as the platform for higher-order Lamb wave devices, showing excellent frequency scalability, low loss, and high k^2. The new COP platforms, a step forward from the previous partial domain inversion piezoelectric platforms [52]–[57], are available thanks to the advance in thin-film bonding technologies. First, the theory for efficient excitation of higher-order Lamb modes in COP platforms is investigated, followed by the design and implementation of both acoustic resonators and ADLs. The resonator shows a 2nd-order symmetric (S2) resonance at 3.05 GHz with a high Q of 657, and a large k^2 of 21.5% and a 6th-order symmetric (S6) resonance at 9.05 GHz with a high Q of 636 and a k^2 of 3.71%, both among the highest demonstrated for gigahertz higher-order Lamb wave LiNbO$_3$ devices. The ADLs show an average IL of 7.5 dB and the lowest reported PL of 0.014 dB/μm at 4.4 GHz for S2. Notable acoustic passbands up to 15.1 GHz are identified. Moreover, the COP platform is readily extendable to other piezoelectric materials. Upon further optimizations, the proposed COP platform can lead to low-loss wideband acoustic components for 5G NR.

The paper is organized as follows. Section II first introduces the theory of higher-order Lamb waves in COP Z-cut LiNbO$_3$. Section III discusses the application of COP thin films, using both the resonators and ADLs. Section IV presents the implemented device. Section V shows the measured results and discussions. Finally, the conclusion is stated in Section VI.

II. HIGHER-ORDER LAMB WAVES IN COMPLEMENTARILY ORIENTED PIEZOELECTRIC PLATFORM

A. Higher-Order Lamb Modes in Piezoelectric Material

Lamb waves are a group of elastic waves in which particles move in the plane defined by the wave vector and the plate normal [58]. Lamb wave solutions can be assorted into two types, namely the symmetrical and antisymmetric modes, based on the symmetry of the motion about the central plane. Within each category, different modes can be further named according to the number of nodal planes (XY planes with X-axis along the lateral direction) in the thickness (Z-axis)
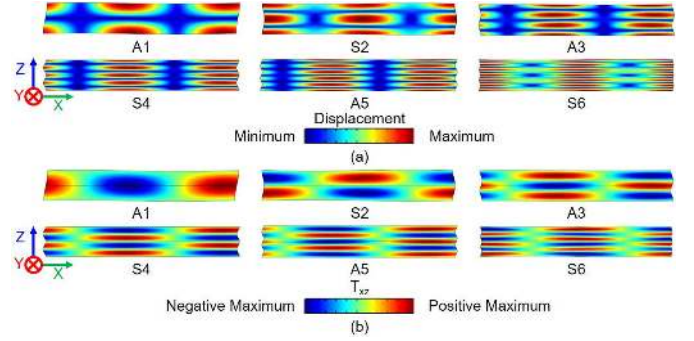

Fig. 1. Vibrational mode shape of higher-order Lamb waves in LiNbO$_3$ thin films, showing (a) displacement, and (b) thickness-shear stress (T_{xz}).

direction [58]. For instance, the displacement of the 1st-order antisymmetric (A1) mode is antisymmetric about the central plane, and one nodal plane can be identified [Fig. 1 (a)]. Similarly, higher-order Lamb modes are named.

More specifically, in RF thin-film piezoelectric devices where the thickness over lateral wavelength ratio (h/λ) is small, Lamb waves can be further classified by the dominant stress component. The thickness-shear (T_{xz}) component is dominant in odd-order antisymmetric modes (e.g., A1) and even-order symmetric modes (e.g., S2). In contrast, the thickness normal stress (T_z) component is dominant in even-order antisymmetric modes (e.g., A2) and odd-order symmetric modes (e.g., S1). The thickness-shear type of Lamb modes excited by top interdigitated electrodes (IDTs) is studied in this work because of the large e_{15} in Z-cut LiNbO$_3$ [42]. Nevertheless, the discussion in Section II can be readily applied to other orientations [59], other piezoelectric materials [33], [60], [61], or devices excited by the thickness electrical fields [27], [62].

The modes of interest (e.g., A1, S2, and A3) are presented in Fig. 1, showing the displacement and T_{xz} within a period. As stated earlier, the number of displacement nodes and stress anti-nodes is the same as the mode order. For plates with small h/λ and electrically short boundary conditions, the resonant frequency of the Nth-order Lamb wave can be approximated by [47]:

$$f_N \approx N/2h \cdot \sqrt{1/(\rho \cdot s_{55}^E)} \tag{1}$$

where ρ is the material density, and s_{55}^E is the thickness-shear compliance constant. One can observe that the center frequency is inversely proportional to the film thickness h and proportional to the mode order N.

To further investigate whether these modes can be excited by lateral electrical fields, the electromechanical coupling (K^2) is calculated using the Berlincourt equation [10], [63] under the quasi-static approximation [58]:

$$K^2 = U_m^2/(U_e \cdot U_d) \tag{2}$$
$$U_m = ((T_i d_{ni} E_n + E_n d_{ni} T_i)/4)dS \tag{3}$$
$$U_e = (T_i s_{ij}^E T_j/2)dS \tag{4}$$
$$U_d = (E_m \epsilon_{mn}^T E_n/2)dS \tag{5}$$

where U_m, U_e, and U_d are the mutual, elastic, and electric energy, respectively. m, n are 1 to 3, while i, j are 1 to 6.
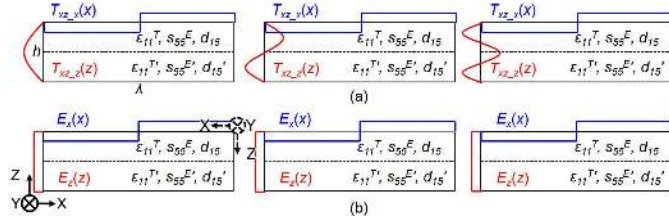
Fig. 2. De-coupled model for calculating K^2 of higher-order Lamb waves excited by lateral electrical fields. (a) Approximated stress and (b) electrical field after separation of variables in the X and Z directions.

Fig. 3. Calculated and simulated center frequency and K^2 of higher-order Lamb modes in different film stacks.

T_i, and E_m are the stress and electrical field elements. d, s^E, and ε^T are the piezoelectric, elastic, and dielectric constants under the strain-charge form. For thickness-shear Lamb modes excited with lateral electrical fields, the corresponding parameters are d_{15}, s_{55}^E, and ε_{11}^T. For plates with small h/λ, the stress fields can be further simplified as [50]:

$$T_{xz}(x, z) = T_{xz0} \cdot T_{xz\_x}(x) \cdot T_{xz\_z}(z) \qquad (6)$$

$$T_{xz\_x}(x) = \mathrm{H}(x - \lambda/2) \qquad (7)$$

$$T_{xz\_z}(z) = sin(N\pi/h \cdot z) \qquad (8)$$

where T_{xz_x} and T_{xz_z} are the decoupled stress fields through the separation of variables in the X and Z directions [Fig. 2 (a)], with the origin defined at the lower-left corner. T_{xz0} is the field amplitude. H() is the Heaviside function. Similarly, the electrical field excited by the top IDTs can be simplified as [50]:

$$E_{xz}(x, z) = E_{xz0} \cdot E_{xz\_x}(x) \cdot E_{xz\_z}(z) \qquad (9)$$

$$E_{xz\_x}(x) = \mathrm{H}(x - \lambda/2) \qquad (10)$$

$$E_{xz\_z}(z) = 1 \qquad (11)$$

where E_{xz_x} and E_{xz_z} are the decoupled electrical fields [Fig. 2 (b)]. E_{xz0} is the amplitude. Using Eqs. 2-11, one can obtain K^2 of the Nth-order Lamb wave (with dominant thickness-shear stress element) excited with IDTs as [10]:

$$K^2 = (8/\pi^2) \cdot d_{15}^2/(s_{55}^E \cdot \epsilon_{11}^T) \cdot 1/N^2 \quad \text{if } N = 1(\text{mod } 2)$$
$$= 0 \quad \text{if } N \neq 1(\text{mod } 2) \qquad (12)$$

where mod() is the modulus function. In Eq. 12, the first term is K^2 for A1, of which the value is determined by the material properties [47]. K^2 of the Nth-order mode decays with N^2, and only the odd-order antisymmetric modes can be excited. Such a conclusion can be explained by visually examing the periodicity and polarity of stress fields along the thickness direction for even and odd-order modes in Fig. 1(b). Assuming a simplified constant E across the thickness of the film, the mutual energy term calculated with Eq. 3 would partially cancel out for the odd-order modes but cancel out for the even-order modes.

In particular, we study the case of 600 nm Z-cut LiNbO₃ as an example. The 600 nm thickness is selected for high operation frequencies beyond 3 GHz while maintaining a high yield for the bonding process. Using Eqs. 1 and 12, A1 is at 2.98 GHz with a K^2 of 30.3%, S2 is at 5.96 GHz with a K^2 of 0, and A3 is at 8.93 GHz with a K^2 of 3.4% (dashed red line in Fig. 3). Therefore, 5G NR bands above 3 GHz require
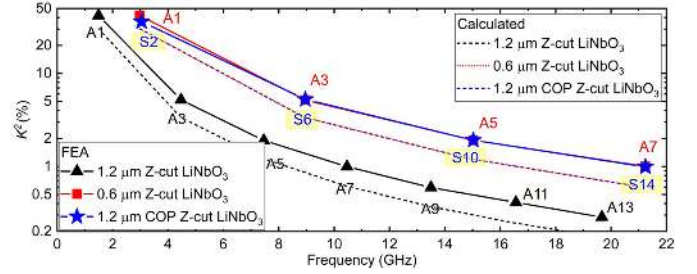
thin LiNbO₃ films less than 600 nm, which leads to higher damping, larger footprint, and worse linearity as introduced in Section I. However, a thicker film (e.g., 1.2 μm Z-cut LiNbO₃, dashed black line in Fig. 3) inevitably leads to diminished K^2 for modes above 3 GHz. Therefore, a new platform with better frequency scalability while maintaining wide bandwidth is of great value.

B. Complementarily Oriented Piezoelectric Platform

To address the challenge, one solution is to tackle the mutual energy cancellation of higher-order Lamb modes through changing the integrated value in Eq. 4. In other words, if the sign of d_{15} is locally flipped in LiNbO₃ while the other parameters (e.g., s_{55}^E, and ε_{11}^T) remain the same, it is feasible to operate at higher-order modes. In the process, one can achieve better frequency scalability while maintaining high K^2. In the implementation, such a platform can be achieved by integrating single-crystal piezoelectric thin films with complementary orientations, which is henceforth referred to as a complementarily oriented piezoelectric (COP) platform in this work.

To quantitatively illustrate the approach, a bi-layer piezoelectric thin film is presented in Fig. 2. Different from the original analysis in Section II-A, we assume the upper and lower half of the thin film have different parameters (d_{15}, s_{55}^E, and ε_{11}^T for the upper half, d_{15}', $s_{55}^{E'}$, and $\varepsilon_{11}^{T'}$ for the lower half). Following the definition of COP, we have $d_{15} = -d_{15}'$, $s_{55}^E = s_{55}^{E'}$, and $\varepsilon_{11}^T = \varepsilon_{11}^{T'}$. K^2 can be calculated through Eqs. 2 – 11, with the only difference in Eq. 3, where the mutual energy U_m across the upper and lower sections is integrated separately. K^2 can then be expressed as:

$$K^2 = (8/\pi^2) \cdot d_{15}^2/(s_{55}^E \cdot \epsilon_{11}^T) \cdot 4/N^2 \quad \text{if } N = 2(\text{mod } 4)$$
$$= 0 \quad \text{if } N \neq 2(\text{mod } 4) \qquad (13)$$

Only a subset of Lamb modes (e.g., S2, S6, S10) can be excited. The conclusion is again visually apparent from the periodicity and polarity of stress fields shown in Fig. 1 (b). Different from the previous case, the mutual energy of the odd-order modes (e.g., A1, A3) across the upper and lower sections entirely cancel out each other. Moreover, the mutual energy in the modes like S4 is internally neutralized in each section. Using Eq. 13, K^2 of a 1.2 μm Z-cut COP LiNbO₃ is plotted as the dashed blue line in Fig. 3, which overlaps with the calculated K^2 of a 0.6 μm Z-cut LiNbO₃ but with

different mode orders. Therefore, it validates that the COP platform has better frequency scalability while maintaining high electromechanical coupling.

Next, we will discuss the feasibility of COP platforms using bonded single-crystal thin films. Different from the conventional approach of sputtering multi-layer tilted c-axis thin films, where the constants are partially modified [64]–[66], bonded piezoelectric thin films [67] enable the implementation of the COP platform through the integration of thin films with different orientations. For Z-cut LiNbO$_3$, which can be notated as a Euler angle of (0°, 0°, 0°) in the Z-X-Z format [68], an additional layer with a Euler angle of (180°, 180°, 0°) satisfies the COP requirements for material constants via matrix rotation [68]. The rotated axis is plotted with dashed lines in Fig. 2, which will be the platform studied in this work. Note that the rotation is not unique. Other rotations, e.g., (0°, 180°, 0°), also satisfy the requirements. (180°, 180°, 0°) is selected because of the current thin-film bonding capabilities.

Moreover, the COP platform may also be applied to film stacks with M layers of piezoelectric films, as long as the alternating layers follow the requirement of COP (same elastic and dielectric constants but different piezoelectric constants). Following the same procedure, one can prove that K^2 of the Nth-order Lamb mode in a stack of M-layer COP structure is:

$$K^2 = \frac{2}{\pi^2} \cdot \frac{d_{15}^2}{s_{55}^E \cdot \epsilon_{11}^T} \cdot \left(\sum_{m=1}^{M} \int_{\frac{(m-1)\pi}{M}}^{\frac{m\pi}{M}} \sin(N\theta + m\pi) \, d\theta \right)^2$$

(14)

It can be proven that the Mth-order mode in an M-layer COP has the same K^2 as that of the first-order Lamb mode in a single layer platform. This leads to even better frequency scalability, although at the cost of introducing additional spurious modes from the residual mutual energy of the lower and higher-order modes that do not entirely cancel out as in the bi-layer COP case.

It is also remarkable that a similar COP approach can be easily extended to other piezoelectric acoustic platforms other than LiNbO$_3$, such as single-crystal lithium tantalate [59]–[61], and doped aluminum nitride [31].

C. Bi-Layer COP Z-Cut Lithium Niobate Thin Film

The analysis in Sections II-A and II-B assumes an ideal quasi-static case where h/λ is near zero, and the electrical and acoustic fields are decoupled [58]. To more accurately study the dispersion relations in LiNbO$_3$, finite element analysis (FEA) in COMSOL is used. The two-dimensional (2D) eigenmode FEA is set up following the steps in [47], [69] for bi-layer 1.2 μm COP Z-cut LiNbO$_3$. Periodic boundary conditions in both the electrical and mechanical domains are applied to the YZ plane. The top and bottom surfaces (XY planes) are set as mechanically free. The electrically open and short boundary conditions are used, respectively. The simulations are performed on the three platforms, namely, 0.6 μm Z-cut LiNbO$_3$, 1.2 μm Z-cut LiNbO$_3$ and 1.2 μm COP Z-cut LiNbO$_3$.

First, the case of a small wavenumber ($\beta = 0.05$ μm^{-1}) is studied and compared to the calculations in Section II-B.

The frequencies of Lamb modes of different mode orders are plotted against K^2 in Fig. 3, which is calculated as [70]:

$$K^2 = (f_{free}^2 - f_{met}^2)/f_{met}^2$$

(15)

where f_{free} and f_{met} are the frequencies of the electrically open and short cases, and f_{free} will be discussed in later discussions. In 0.6 μm Z-cut LiNbO$_3$, A1 is calculated at 2.98 GHz with a K^2 of 41.9%, S2 is at 5.95 GHz with a K^2 of 0, and A3 is calculated at 8.96 GHz with a K^2 of 5.18% (red squares in Fig. 3). For 1.2 μm Z-cut LiNbO$_3$, f_{free} is halved, but K^2 remains the same (black triangles in Fig. 3). For 1.2 μm COP Z-cut LiNbO$_3$, A1 is calculated at 1.49 GHz with a K^2 of 0, S2 is calculated at 3.05 GHz with a K^2 of 0, and A3 is calculated at 4.47 GHz with a K^2 of 0. The results agree with the calculated values, with the slight discrepancies likely due to the introduced assumptions. Such a result validates the effectiveness of the COP designs.

Next, the dispersions of higher-order Lamb waves are studied for actual implementations of both resonant and non-resonant acoustic devices in COP platforms. The frequencies of higher-order Lamb waves with different β (between 0.05 μm^{-1} and 4 μm^{-1}) for 1.2 μm COP Z-cut LiNbO$_3$ under the electrically short condition are shown in Fig. 4 (a). Cut-off frequencies (f_c) are observed for these modes [47], and the frequencies increase with larger β. In comparison, the dispersion of 0.6 μm Z-cut LiNbO$_3$ under the same conditions are plotted with dashed lines in Fig. 4 (a). The Nth-order curve overlaps with the 2Nth-order dispersion curves in COP LiNbO$_3$ well, with the slight difference caused by the different h/λ in the two cases.

Another critical parameter is K^2 of the higher-order Lamb waves at different β, determining the transduction efficiency with various transducer designs. The results calculated using Eq. 15 is plotted in Fig. 4 (b). High K^2 over 35% can be observed for S2 waves with a long λ (or with operation frequencies close to f_c). K^2 declines for A1 waves at a higher frequency (or with a larger h/λ). Similarly, S6 mode follows the same trend, but with a smaller K^2. Another observation is that with a larger β beyond 1.2 μm^{-1}, higher-order Lamb waves other than S2 and S6 can be efficiently excited, showing K^2 over 1%, because the electrical field cannot penetrate the entire thickness due to a larger h/λ, causing insufficient cancellation of the mutual energy (Eq. 3).

Finally, the phase velocity (v_p) and the group velocity (v_g) are obtained by [58]:

$$v_p = 2\pi f/\beta$$

(16)

$$v_g = 2\pi \cdot \partial f/\partial \beta$$

(17)

The obtained values are plotted in Fig. 4 (c) and (d) for the electrically short case. Higher-order Lamb waves feature high v_p (above 10 km/s), and low v_g (below 5 km/s) simultaneously, which can be leveraged to build high-frequency devices with large feature sizes, while allowing long group delay with a compact structure [47]. These characteristics promise COP LiNbO$_3$ as a suitable acoustic platform for 5G NR applications.

In Section II, the fundamentals of higher-order Lamb waves in COP acoustic platforms have been discussed. Bi-layer COP
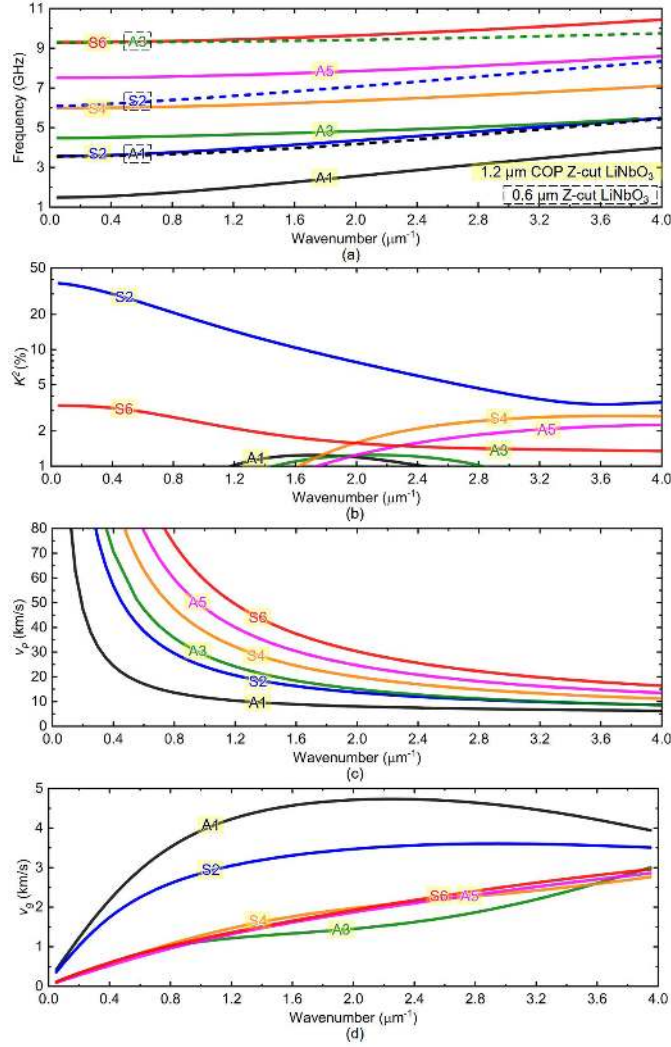
Fig. 4. FEA simulated characteristics of higher-order Lamb waves with different wavenumber in an 1.2 μm thick COP Z-cut LiNbO$_3$ thin film. (a) Frequency with electrically short boundary conditions, (b) K^2. (c) v_p, and (d) v_g with electrically short boundary conditions.

Z-cut LiNbO$_3$ has been validated for efficient piezoelectric transduction for 5G NR above 3 GHz, showing large K^2 and v_p simultaneously. Based on such a platform, both resonant and non-resonant devices will be designed in Section III to showcase the design flexibility of COP platforms as a universal solution for high-frequency acoustics.

III. DESIGN OF HIGHER-ORDER LAMB WAVE DEVICES

A. Complementarily Oriented Bi-Layer Acoustic Resonator

The mockup view of a typical complementarily oriented bi-layer acoustic resonator (COBAR) is shown in Fig. 5 with the key parameters explained in Table I. The resonator is composed of 300 nm thick aluminum (Al) interdigitated electrodes (IDTs) on the top of a suspended 1.2 μm COP Z-cut LiNbO$_3$ thin film. The orientations of the upper and lower layers are labeled in the front view, following the definition in Section II-C (Fig. 2). The LiNbO$_3$ thickness is selected for setting the resonance above 3 GHz for 5G NR bands [44],
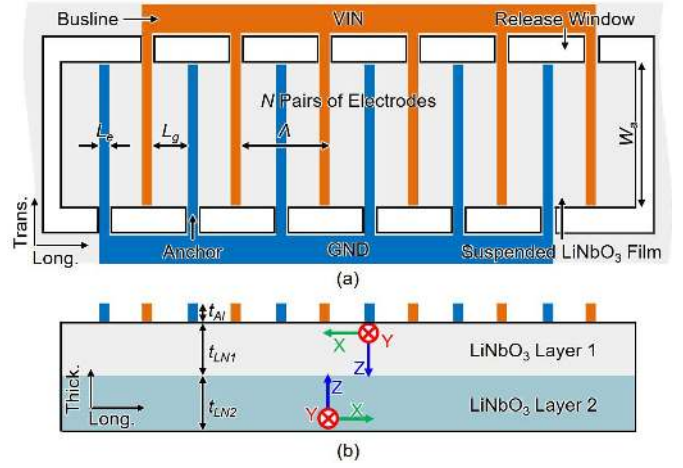

Fig. 5. Mockup of a COBAR in a suspended COP Z-cut LiNbO$_3$ thin film. (a) Top view. (b) Front view.

TABLE I
DESIGN PARAMETERS OF COBAR

Sym.	Parameter	Value	Sym.	Parameter	Value
Λ	Cell length (μm)	50	W_a	Aperture width (μm)	65
L_e	Electrode length (μm)	2.5	W_r	Release window width (μm)	8
L_g	Gap length (μm)	22.5	t_{LN}	LiNbO$_3$ thickness (nm)	600
N	No. of electrode pairs	11	t_{Al}	Aluminum thickness (nm)	300

and the Al thickness is selected for reducing the electrical loading [17], [47]. The cell length (Λ) is set as 50 μm for higher coupling (Fig. 4). The electrode width (L_e) is 2.5 μm for a small ratio of L_e/Λ to mitigate spurious modes [48]. Additional piezoelectric slabs with a width of $\Lambda/2$ are placed on the sides for keeping the periodicity. The bus lines are placed outside the resonant body for reducing the feedthrough capacitance.

2D frequency-domain FEA is used to validate the expected higher-order Lamb modes with significant k^2 at higher frequencies. An airbox is included surrounding the resonator to include the effects of the capacitive feedthrough between the IDTs in air, which will reduce the available k^2 of the COBAR. Mechanical Q is set as 500 based on previous experimental results in similar film stacks [44]. The wideband admittance response between 0 and 24 GHz is presented in both amplitude [Fig. 6 (a)] and phase [Fig. 6 (b)]. As derived in Section II-B (Eq. 13) and simulated in Section II-C (Fig. 3), only a subsection of the higher-order Lamb modes (e.g., S2, S6, S10) are excited. The vibrational mode shape of S2 is shown in Fig. 6 (c) in both displacement and stress T_{xz} (scaled in Z-direction), showing the alternating stress distribution in both X and Z-directions. The zoomed-in admittance response is shown in Fig. 7 (a) – (f) for S2, S6, and S10. The perceived k^2 of each mode is calculated as [70]:

$$k^2_{perceived} = \pi^2/8 \cdot [(f_p/f_s)^2 - 1] \tag{18}$$

where f_s and f_p are the resonance and anti-resonance defined as the frequency point with the minimum and maximum
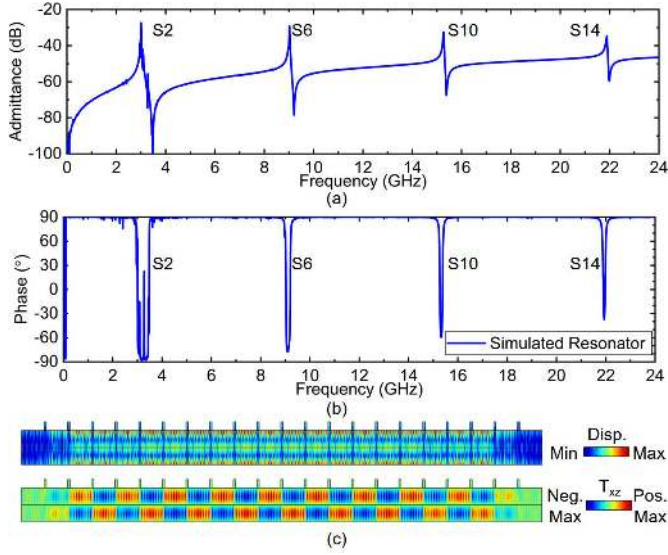
Fig. 6. FEA simulated results of the COBAR. Simulated wideband admittance response in (a) amplitude and (b) phase. (c) Simulated displacement and stress mode shape at the S2 resonance.
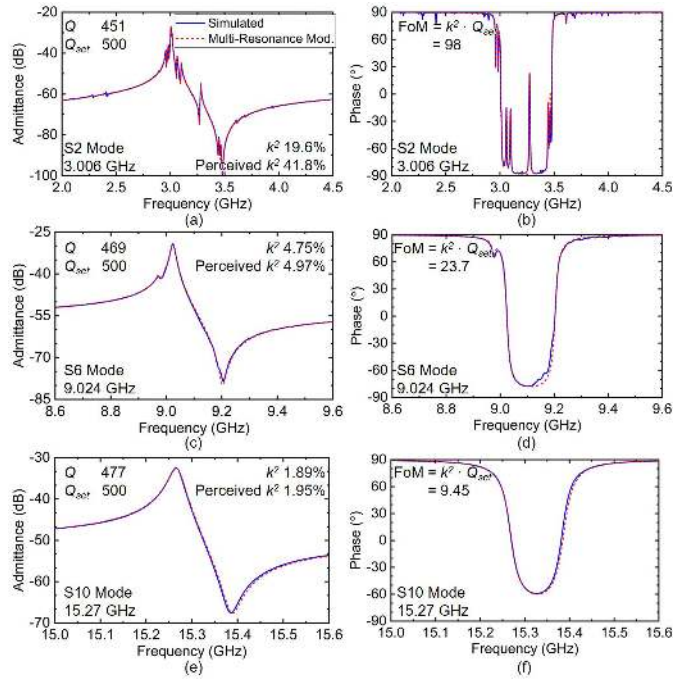

Fig. 7. Zoomed-in simulation and multi-resonance MBVD fitted admittance response in amplitude and phase of (a) (b) S2, (c) (d) S6, and (e) (f) S10.

impedance. S2 has a perceived k^2 of 41.8% at 3.006 GHz. On the other hand, S6 and S10 have perceived k^2 of 4.97% and 1.95% at 9.024 GHz and 15.27 GHz, respectively. The obtained f_s and perceived k^2 agree with those extracted from eigenmode FEA in Section II-C (Fig. 4), with the slight reduction caused by the capacitive coupling between IDTs. More specifically, out of the total static capacitance (C_0) of 32.9 fF, 6.8 fF is introduced by the capacitance in air, which can be mitigated using devices with a slightly smaller Λ. One issue of the current prototype is the in-band spurious modes. They originate from higher-order overtones of fundamental modes
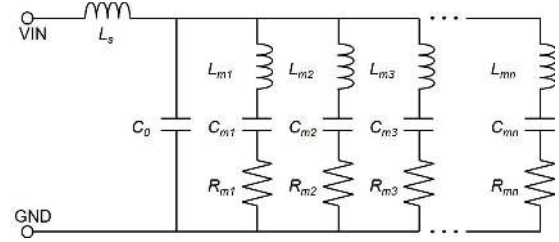

Fig. 8. Multi-resonance MBVD model for extracting key parameters.

TABLE II
EXTRACTED KEY PARAMETERS FROM COBAR SIMULATION

Sym.	Value	Sym.	Value	Sym.	Value
C_0	32.9 fF	L_s	0 nH	n	14
f_{s1}	**3.01 GHz**	k_1^2	**19.6%**	Q_1	**451**
f_{s2}	3.02 GHz	k_2^2	8.89%	Q_2	445
f_{s3}	2.98 GHz	k_3^2	4.49%	Q_3	500
f_{s4}	2.96 GHz	k_4^2	3.53%	Q_4	482
f_{s5}	3.06 GHz	k_5^2	2.82%	Q_5	408
f_{s6}	3.10 GHz	k_6^2	2.00 %	Q_6	413
f_{s7}	3.28 GHz	k_7^2	0.61%	Q_7	495
f_{s8}	3.45 GHz	k_8^2	0.03%	Q_8	460
f_{s9}	3.47 GHz	k_9^2	0.02%	Q_9	462
f_{s10}	3.61 GHz	k_{10}^2	0.01%	Q_{10}	584
f_{s11}	**9.02 GHz**	k_{11}^2	**4.75%**	Q_{11}	**469**
f_{s12}	8.97 GHz	k_{12}^2	0.22%	Q_{12}	699
f_{s13}	**15.3 GHz**	k_{13}^2	**1.89%**	Q_{13}	**477**
f_{s14}	21.9 GHz	k_{14}^2	0.99%	Q_{14}	499

(A0, S0), higher-order overtones of S2, and mode conversion at the edge reflectors. The spurious mode suppression will be an essential topic in future works on optimizing COP platforms.

To accurately extract the key parameters of each mode, a multi-branch MBVD model has been used (Fig. 8), which has been shown critical for devices with large k^2 [71]. Each motional branch represents one acoustic mode, and the motional elements are defined as [71]:

$$R_{mi} = \pi^2/8 \cdot 1/(\omega_{si} C_0 k_i^2 Q_i) \tag{19}$$
$$L_{mi} = \pi^2/8 \cdot 1/(\omega_{si}^2 C_0 k_i^2) \tag{20}$$
$$C_{mi} = 8/\pi^2 \cdot C_0 k_i^2 \tag{21}$$

where R_{mi}, L_{mi}, and C_{mi} are the motional resistance, inductance, and capacitance, ω_{si} is the angular resonant frequency, k_i^2 is the effective electromechanical coupling coefficient, and Q_i is the quality factor for the branch with an index of i. A series inductance L_s is included for modeling the IDT inductance in the measurement [50]. Following the recursive procedure in [71], the key parameters are extracted, listed in Table II, and also plotted in Fig. 7. k^2 of S2 is 19.6% (mode 1 in Table II), because of the adjacent high k^2 S2 overtones and undertones (modes 2-10 in Table II). These modes
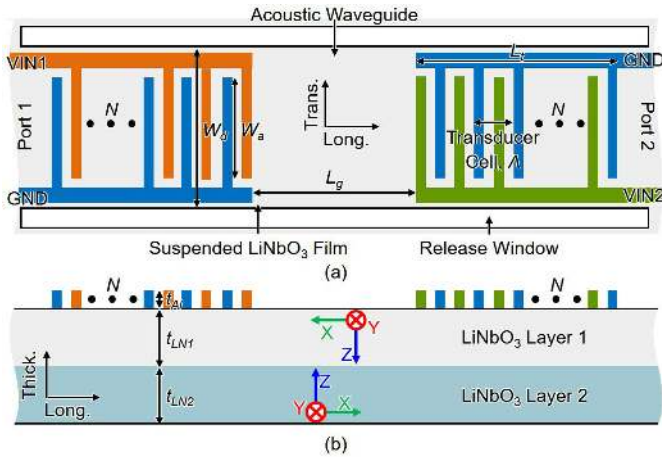
Fig. 9.   Mockup of a COB-ADL in a suspended COP Z-cut LiNbO$_3$ thin film. (a) Top view. (b) Front view.

TABLE III
DESIGN PARAMETERS OF COB-ADLS

Sym.	Parameter	Value	Sym.	Parameter	Value
Λ	Cell length (µm)	2.4	W_a	Aperture width (µm)	50
N	Number of cells	4	W_d	Device width (µm)	74
L_g	Gap length (mm)	0.02-1.28	t_{LN}	LiNbO$_3$ thickness (nm)	600
L_t	Transd. length (µm)	9.6	t_{Al}	Aluminum thickness (nm)	50

exist because of the thick Al in this work [48], which aims to lower the electrical loading for exposing Q of the COP platform. k^2 of S6 is 4.75% (mode 11 in Table II), and k^2 of S10 is 1.89% (Mode 13 in Table II), both showing a clean spectrum and high k^2.

To conclude, COBAR has been designed in this subsection, further validating the advantages of large k^2 and the excellent frequency scalability of COP LiNbO$_3$ platforms. Q of COBARs will be experimentally studied in Section V-A.

B. Complementarily Oriented Bi-Layer Acoustic Delay Lines

The mockup view of a typical complementarily oriented bi-layer acoustic delay line (COB-ADL) is shown in Fig. 9 with the key parameters explained in Table III. The COB-ADL is composed of 50 nm thick Al IDTs on the top of a suspended 1.2 µm COP Z-cut LiNbO$_3$ thin film. The orientations of the upper and lower layers are labeled in the front view, following the definition in Section II-C (Fig. 2). A pair of bi-directional transducers are placed on the two longitudinal ends of the ADL with a gap length of L_g (between 0.02 mm and 1.28 mm), including 4 cells of IDTs. A cell length Λ of 2.4 µm is selected to avoid the cut-off phenomenon [47], while efficiently exciting various higher-order Lamb modes (Fig. 4). Considering both the wave diffraction and the electrical loading [47], the aperture width (W_a) is set to 50 µm. In operation, EM signals sent in Port 1 are converted into acoustic waves through piezoelectricity, propagating to Port 2 before being converted back to the EM domain.
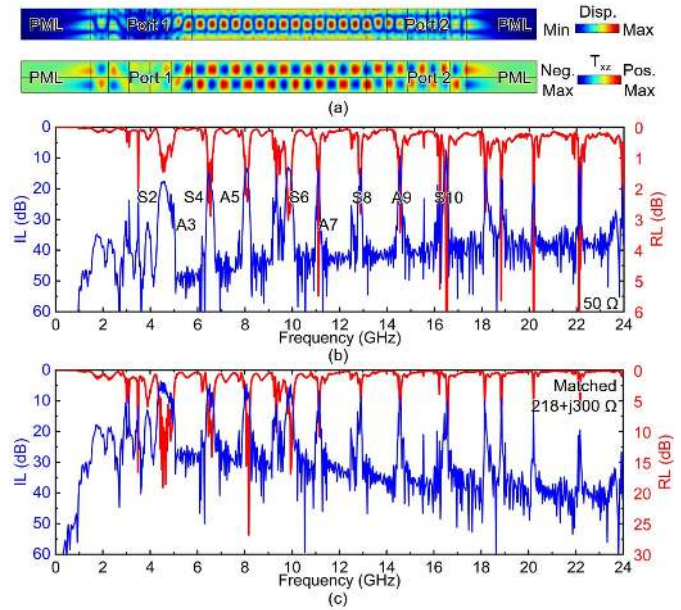

Fig. 10.   (a) Simulated vibrational mode shapes in the S2 passband. Simulated wideband IL and RL of the COB-ADL under (b) 50 Ω, and (c) conjugately matched to the S2 band conditions.

To validate the COB-ADL design, 2D frequency-domain FEA is set up following the reported procedure in [47]. As shown in Fig. 10 (a), a pair of transducers are included in the simulation, with the perfectly matched layers (PMLs) placed on the longitudinal ends to suppress the reflections. The structure is assumed lossless because the loss in the new COP LiNbO$_3$ is unknown. The simulated vibrational mode shapes [Fig. 10 (a)] within the S2 passbands confirm that acoustic waves are efficiently excited and propagate outside of the transducers.

The wideband IL and return loss (RL) are plotted in Fig. 10 (b) with both ports terminated with 50 Ω. Note that a feedthrough capacitance of 1 fF is included between ports, according to the measured results in prior ADL implementations [47]. The passbands of different higher-order Lamb modes are labeled. Pronounced passbands between S2 and S10 can be observed between 4.55 GHz and 16.5 GHz, except A3, whose K^2 diminishes as predicted by Fig. 4. An IL of 17.5 dB and a 3-dB FBW of 6.16% are obtained for S2 at 4.55 GHz. An IL of 14.5 dB and a 3-dB FBW of 1.42% are obtained for S4 at 6.46 GHz. The key parameters for other bands are listed in Table IV. The higher frequency bands (above A3) are previously unattainable because they suffer from significant mode cut-off in the conventional Z-cut LiNbO$_3$ [51], and enabled by the COP platform. Another observation is that the higher-order modes have less 3-dB FBW, which is caused by lower K^2 of those modes [72].

For the lossless simulation, the IL includes a 6-dB bi-directional loss [72], [73], and the additional loss caused by the port impedance mismatch. To verify, the performance is conjugately matched to 218+j300 Ω based on the S2 band, using Keysight Advanced Design System (ADS) [Fig. 10 (c)]. Interestingly, the adjacent bands (S4, A5, and S6) are also

TABLE IV
EXTRACTED KEY PARAMETERS FROM COB-ADL SIMULATION

Mode	50 Ω			Matched to S2		
	f_c	IL	FBW	f_c	IL*	FBW
S2	4.55 GHz	17.5 dB	6.16%	4.55 GHz	5.6 dB	9.31%
S4	6.46 GHz	14.5 dB	1.42%	6.54 GHz	7.6 dB	4.36%
A5	8.06 GHz	13.4 dB	1.76%	8.10 GHz	7.8 dB	2.74%
S6	9.85 GHz	13.1 dB	1.81%	9.91 GHz	7.5 dB	2.01%
A7	11.1 GHz	13.8 dB	0.52%	11.1 GHz	13.6 dB	1.24%
S8	12.9 GHz	13.2 dB	0.31%	12.9 GHz	13.7 dB	0.60%
A9	14.6 GHz	9.36 dB	0.19%	14.6 GHz	12.0 dB	0.71%
S10	16.5 GHz	7.68 dB	0.21%	16.6 GHz	16.4 dB	0.49%

* Average IL for the matched case that has mitigated effects from multi-reflections.

matched. This is because the lower K^2 of higher-order modes (Fig. 4) are compensated by a higher operating frequency (f_c), which leads to similar radiation conductance at different bands [74]. For future works, 50 Ω ADLs can be designed by sizing the transducers and including series inductors. Note that more pronounced ripples can be observed under the conjugate matched case, caused by a reduced IL for the triple transit echo (TTE) from the bi-directional transducers [72]. The ripples will be less severe for actual implementation because of the existence of the acoustic propagation loss (PL). To mitigate the effects of the multi-reflections for benchmarking the COB-ADL performance, the average IL and 3-dB FBW are obtained from the smoothed transmission (400-point-window from measured data). An average IL of 5.6 dB and a 3-dB FBW of 9.31% are obtained for S2 at 4.55 GHz. An average IL of 7.6 dB and a 3-dB FBW of 4.36% are obtained for S4 at 6.46 GHz. The values are close to the predicted 6 dB, with a slight difference due to the in-band ripples. The parameters for other bands are listed in Table IV.

Next, COB-ADLs with different L_g are simulated for extracting the major propagation parameters (e.g., v_g and PL) of the higher-order Lamb waves. COB-ADLs with L_g of 20, 40, and 80 μm are simulated. IL, RL, and group delay are plotted in Fig. 11 with both ports terminated with 50 Ω. The passbands for Lamb waves of different orders are highlighted. Comparing the performance between devices with different L_g, three major differences can be found. First, devices with different L_g show the same IL, because the acoustic waveguide is assumed lossless. However, the difference in IL in the actual implementation can be used to extract PL. Second, the frequency spacing between the in-band ripples of the shorter devices is larger because of a longer resonant cavity between the transducers for triple transit interference [69]. Third, longer devices show longer group delays, and the difference can be used to extract v_g. v_g of S2 and S4 are extracted through linear regression and plotted in Fig. 12, showing v_g around 3.5 km/s for S2 at 4.55 GHz, and v_g around 1.8 km/s for S4 at 6.40 GHz. The results agree well with that directly obtained from eigenmode FEA (Section II-C).
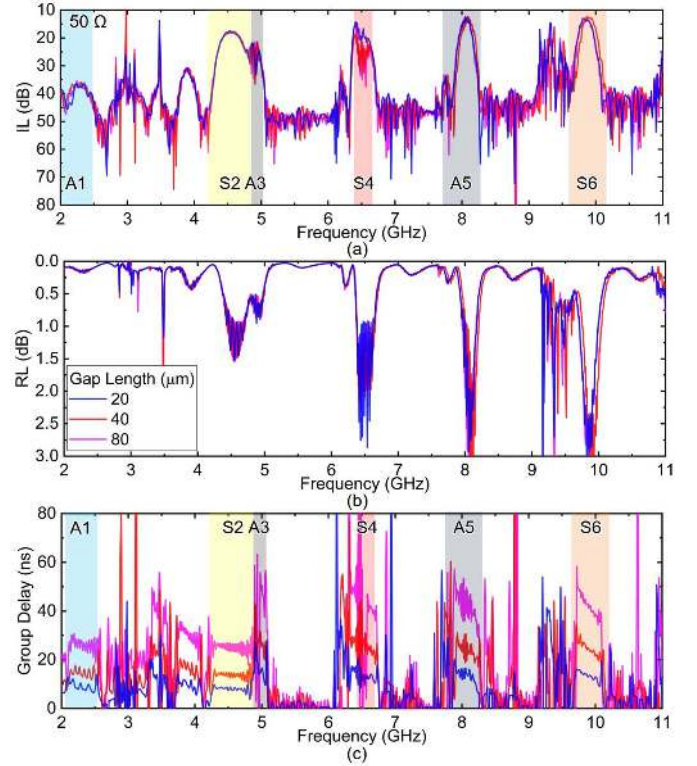

Fig. 11.   Simulated (a) IL, (b) RL, and (c) group delay of COB-ADLs with different L_g of 20, 40, and 80 μm, but the same transducer design (Table III).
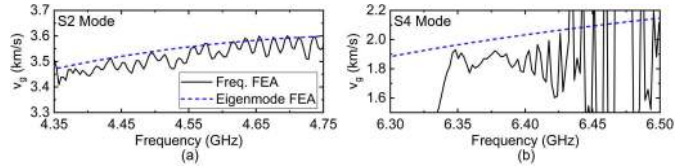

Fig. 12.   Extracted group velocity in comparison with that directly obtained from the eigenmode simulations for (a) S2, and (b) S4.

Note that the low coupling resonances between the transducers in the lossless simulation generate severe ripples, but their effects will be mitigated in the actual measurement with PL.

To sum up, in Section III, both the resonant devices (COBARs) and non-resonant devices (COB-ADLs) have been designed in the proposed bi-layer COP Z-cut LiNbO$_3$. The simulated results confirm the feasibility of implementing high-performance higher-order Lamb wave devices in such a platform. The implementation of the showcased testbeds will be presented in Section IV.

IV. HIGHER-ORDER LAMB WAVE DEVICE IMPLEMENTATION

The devices were implemented following the fabrication process reported in [48]. The 1.2 μm bi-layer COP Z-cut LiNbO$_3$ thin film on a 4-inch silicon (Si) wafer is provided by NGK Insulators, Ltd. The process starts with defining the release windows via inductively coupled plasma reactive-ion etching (ICP-RIE). Al electrodes are then deposited with evaporation and lift off. As the last step, the structures are released with xenon difluoride (XeF$_2$).
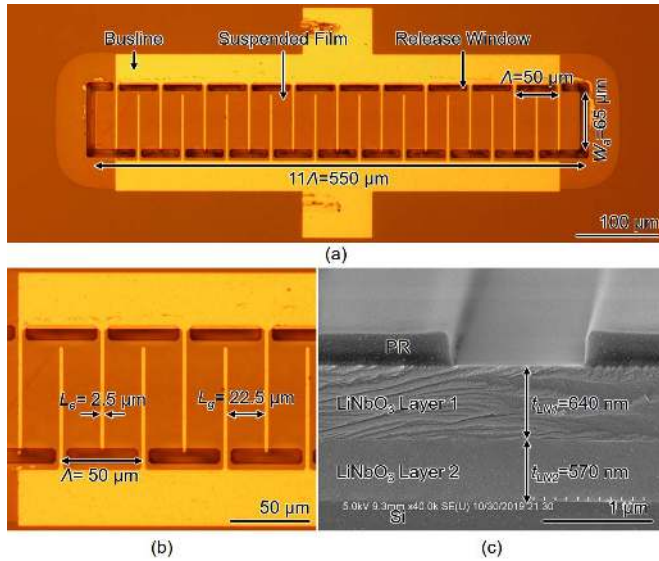
Fig. 13. (a) Zoomed-out and (b) zoomed-in optical images of the fabricated COBAR. (c) SEM image of the cross-section of the COP LiNbO$_3$. The dimensions are listed in Table I.
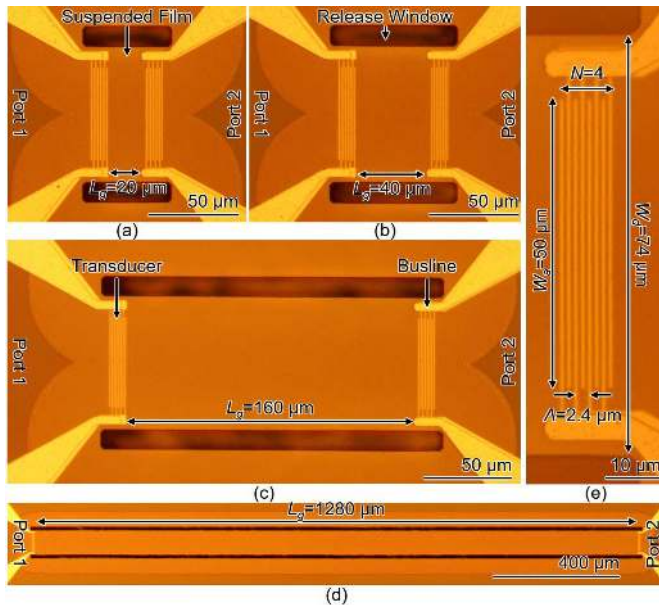

Fig. 14. Zoomed-out optical images of the fabricated COB-ADL with L_g of (a) 20 μm, (b) 40 μm, (c) 160 μm, (d) 1280 μm. (e) Zoomed-in optical image of the bi-directional transducer. The dimensions are listed in Table III.

The zoomed-out and zoomed-in optical images of the fabricated COBAR are shown in Fig. 13 (a) (b) with the dimensions listed in Table I. The device shows well defined IDTs and release windows. Another device with the exact design but without the resonant body is implemented for obtaining the capacitive feedthrough from the probing pads. The optical images of the build COB-ADLs are presented in Fig. 14 (a) – (e), with the dimensions listed in Table III.

The cross-section of the COP Z-cut LiNbO$_3$ on Si wafer is shown in Fig. 13 (c), with a top layer of 640 nm and a bottom layer of 570 nm. The stripes in the cross-section are
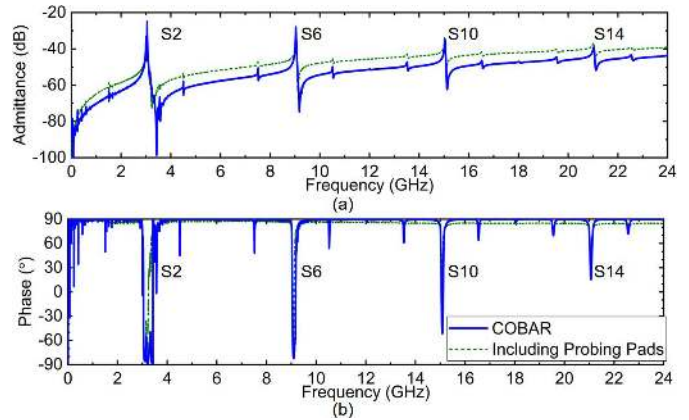

Fig. 15. Measured wideband admittance responses in (a) amplitude and (b) phase for both the resonator and its response excluding the feedthrough from the probing pads.

caused by the wafer cleaving. The slight deviation from the designed thickness will affect the performance of the higher-order modes, which will be presented in Section V.

V. MEASUREMENT AND DISCUSSION

A. Complementarily Oriented Bi-Layer Acoustic Resonator

The fabricated COBAR was measured with an Agilent N5230A network analyzer at the −10 dBm power level in the air. The wideband admittance response between 0 and 24 GHz is presented in both amplitude [Fig. 15 (a)] and phase [Fig. 15 (b)]. The effects of the probing pads are removed through subtracting the measured feedthrough. As simulated in Section II-A (Fig. 6), a subsection of the higher-order Lamb modes (e.g., S2, S6, and S10) are effectively excited. However, different from the simulation (Fig. 6), other higher-order modes are also excited, especially at higher frequencies. It is caused by the slight difference in the thickness of the two layers in COP Z-cut LiNbO$_3$ [Fig. 13 (c)], which leads to insufficient cancellation of the mutual energy of these modes (Section II-B). Such non-ideality limits the ultimate operation frequency below 20 GHz, and can be further improved through film trimming [75]. Nevertheless, the examined modes (S2, S6, and S10) show much larger k^2 than Lamb modes with other mode orders.

The zoomed-in admittance is shown in Fig. 16 for S2, S6, and S10, respectively. The multi-resonance model [71] (Fig. 8) is plotted in Fig. 16 with dashed lines and its key parameters are also listed in Table V. The S2 resonance at 3.049 GHz shows a perceived k^2 of 32.9% (Eq. 4) and a 3-dB Q of 1219 [Fig. 16 (a) (b)]. The extracted k^2 is 22.8%, and the extracted Q is 657. The results agree well with the simulated values (Fig. 7). Similarly, the degradation from the perceived k^2 is due to the existence of the in-band spurious modes (Modes 2-9 in Table V). Compared to prior A1 mode resonators in conventional Z-cut LiNbO$_3$ above 3 GHz [38]–[40], the S2 mode resonator in the COP platform shows an improved Q (above 600) with a similar k^2 (above 20%). The S6 resonance at 9.045 GHz shows a perceived k^2 of 3.80% and a 3-dB Q of 660 [Fig. 16 (c) (d)]. The extracted k^2 is 3.71%,
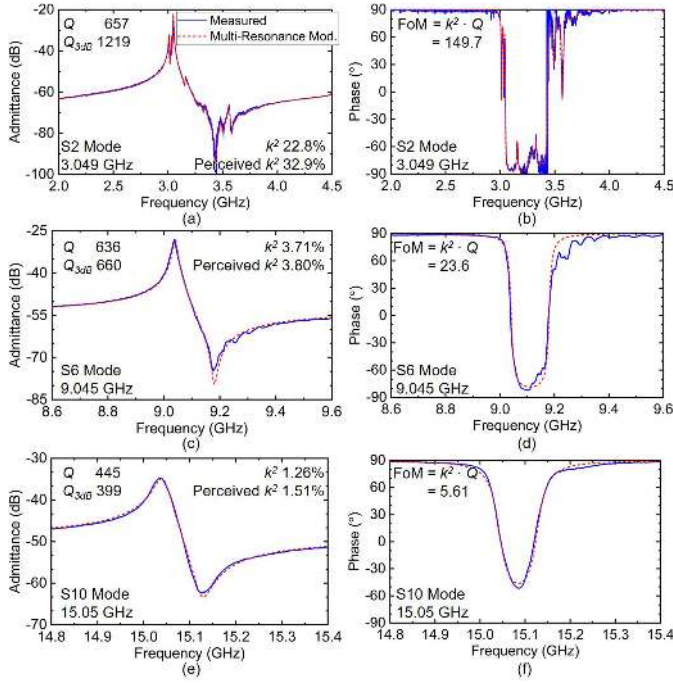
Fig. 16. Zoomed-in measurement and multi-resonance MBVD fitted admittance response in amplitude and phase of (a) (b) S2, (c) (d) S6, and (e) (f) S10.
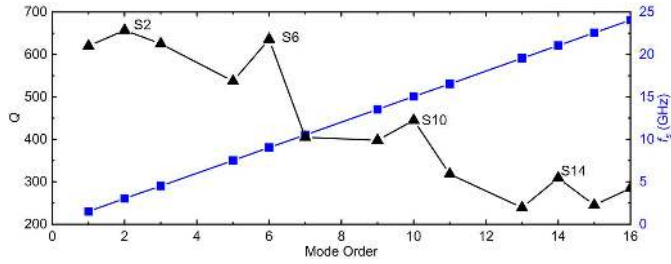

Fig. 17. Extracted Q and f_s of higher-order Lamb modes in the COBAR.

TABLE V
EXTRACTED KEY PARAMETERS FROM COBAR MEASUREMENTS

Sym.	Value	Sym.	Value	Sym.	Value
C_0	34.6 fF	L_s	0.25 nH	n	21
f_{s1}	**3.05 GHz**	k_1^2	**22.8%**	Q_1	**657**
f_{s2}	3.01 GHz	k_2^2	7.26%	Q_2	482
f_{s3}	3.03 GHz	k_3^2	5.35%	Q_3	581
f_{s4}	3.16 GHz	k_4^2	0.82%	Q_4	238
f_{s5}	3.29 GHz	k_5^2	0.49%	Q_5	71.4
f_{s6}	3.33 GHz	k_6^2	0.14%	Q_6	231
f_{s7}	3.49 GHz	k_7^2	0.13%	Q_7	186
f_{s8}	3.56 GHz	k_8^2	0.31%	Q_8	214
f_{s9}	3.68 GHz	k_9^2	0.14%	Q_9	65
f_{s10}	1.51 GHz	k_{10}^2	0.21%	Q_{10}	620
f_{s11}	4.51 GHz	k_{11}^2	0.15%	Q_{11}	625
f_{s12}	7.52 GHz	k_{12}^2	0.19%	Q_{12}	537
f_{s13}	**9.04 GHz**	k_{13}^2	**3.71%**	Q_{13}	**636**
f_{s14}	10.52 GHz	k_{14}^2	0.18%	Q_{14}	405
f_{s15}	13.53 GHz	k_{15}^2	0.12%	Q_{15}	398
f_{s16}	**15.05 GHz**	k_{16}^2	**1.26%**	Q_{16}	**445**
f_{s17}	16.54 GHz	k_{17}^2	0.15%	Q_{17}	318
f_{s18}	19.56 GHz	k_{18}^2	0.16%	Q_{18}	239
f_{s19}	21.05 GHz	k_{19}^2	0.49%	Q_{19}	309
f_{s20}	22.56 GHz	k_{20}^2	0.13%	Q_{20}	245
f_{s21}	24.05 GHz	k_{21}^2	0.04%	Q_{21}	285

and the extracted Q is 636 (Mode 13 in Table V). The S10 resonance at 15.05 GHz shows a perceived k^2 of 1.51% and a 3-dB Q of 399 [Fig. 16 (c) (d)]. The extracted k^2 is 1.26%, and the extracted Q is 445 (Mode 16 in Table V). The obtained Q above 600 at 9 GHz and Q above 400 at 15 GHz are also higher than the reported results in the conventional LiNbO$_3$ thin films [38]–[40]. Therefore, the results validate our earlier assumption that the thicker film of COP platforms not only have better frequency scalability but also feature lower loss, likely due to reduced surface losses because of a reduced surface-area-to-volume ratio [15], [16].

Finally, to further analyze the damping of higher-order Lamb modes in the COP platform, the extracted Q and f_s of higher-order Lamb modes (Modes 1, 10 – 21 in Table V) with different mode orders are shown in Fig. 17. The resonant frequency is linearly proportional to the mode order, with a frequency spacing of 1.503 GHz for the adjacent modes. The higher-order modes, within the same resonant body, present a declining Q at higher frequencies, from around 600 below 10 GHz (A1 to S6) to about 200 above 20 GHz

(A13 to S16). The result that the higher-order Lamb waves show higher damping might be caused by a combination of more significant electrical [43] and mechanical [15] damping at higher frequencies.

The obtained performance is compared to the previously reported acoustic resonators operating above 3 GHz (Table IV), including SAW [25], IHP SAW [25], longitudinal leaky SAW (LLSAW) [24], [25], FBAR [29], and higher-order Lamb wave devices in conventional single-layer structures [25], [40], [44], [50]. f_s, k^2, and Q are listed, along with the piezoelectric film thickness and feature sizes. The perceived k^2 of different reports are calculated using Eq. 18 for a fair comparison (consistent with Eq. 21). Note that the maximum Bode Q is reported by a few references [24], [25], [29], which is generally much larger than Q extracted from the resonance [76]. Compared to other technologies, the COP LiNbO$_3$ platform has the advantages of the thin-film Lamb wave devices, achieving high k^2 and high f_s with a large feature size. Moreover, compared to other thin-film devices, the COP platform features higher Q and better frequency scalability. Therefore, we have validated the predicted advantages of excellent frequency scalability, low loss, and high coupling in the COP LiNbO$_3$ platform. Note that, although demonstrating a record-high Q for thin-film Lamb wave resonators above

TABLE VI

REPORTED ACOUSTIC RESONATORS ABOVE 3 GHz

Ref.	Piezo. Thick.	Feature Size	f_s	Perceived k^2*	Q	Comment
[25]	bulk	N/A	3.4 GHz	13.9%	600**	SAW
[25]	0.36 μm	0.275 μm	3.4 GHz	9.0%	1750**	IHP-SAW
[25]	0.34 μm	0.425 μm	3.5 GHz	24.7%	660**	LLSAW
[25]	0.24 μm	0.3 μm	5.0 GHz	24.2%	565**	LLSAW
[25]	0.395 μm	0.45 μm	5.4 GHz	34.4%	590**	Thin-Film
[29]	0.42 μm	N/A	5.4 GHz	12.0%	1400**	FBAR
[44]	0.5 μm	0.5 μm	4.0 GHz	28.0%	420***	Thin-Film
[40]	0.5 μm	0.4 μm	4.8 GHz	31.2%	70***	Thin-Film
[29]	0.4 μm	3.0 μm	12.9 GHz	3.7%	224***	Thin-Film
[29]	0.4 μm	3.0 μm	21.4 GHz	1.5%	287***	Thin-Film
[29]	0.4 μm	3.0 μm	29.9 GHz	0.9%	328***	Thin-Film
S2	**1.2 μm**	**2.5 μm**	**3.0 GHz**	**32.9%**	**657***	**Thin-Film**
S6	**1.2 μm**	**2.5 μm**	**9.0 GHz**	**3.8%**	**636***	**Thin-Film**
S10	**1.2 μm**	**2.5 μm**	**15.1 GHz**	**1.5%**	**445***	**Thin-Film**

* Perceived k^2 of different reports are calculated using Eq. 18
** Reported maximum Bode Q is listed
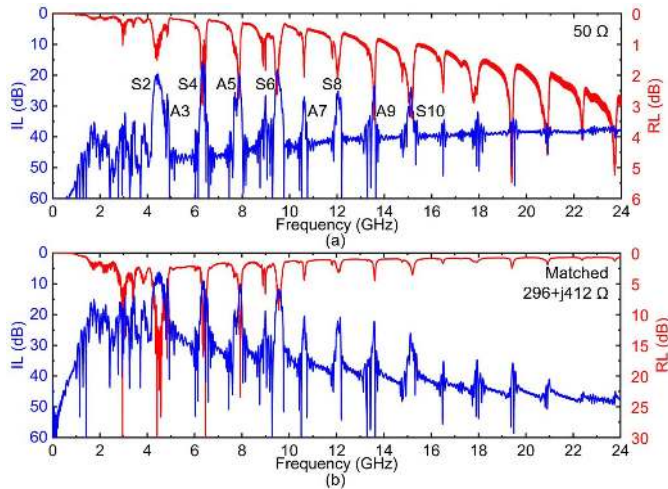*** Reported loaded Q at the resonance

Fig. 18. Measured wideband IL and RL of the COB-ADL under (a) 50 Ω, and (b) conjugately matched to the S2 band conditions.

3 GHz, the performance of the prototype COBAR is far from the full potential of the platform. Upon design optimizations, COBARs with k^2 above 30%, Q above 600 for S2, and mitigated spurious modes can be expected.

B. Complementarily Oriented Bi-Layer Acoustic Delay Lines

The fabricated COB-ADLs were measured with an Agilent N5230A network analyzer at the −10 dBm power level in the air. The wideband IL and return loss (RL) are plotted in Fig. 18 (a) with both ports terminated with 50 Ω. As simulated in Fig. 10 (a), the passbands of different higher-order Lamb modes are obtained from S2 to

TABLE VII

EXTRACTED PARAMETERS FROM COB-ADL MEASUREMENTS

Mode	50 Ω			Matched to S2		
	f_c	IL	FBW	f_c	IL*	FBW
S2	4.41 GHz	19.7 dB	5.08%	4.46 GHz	7.5 dB	7.55%
S4	6.32 GHz	15.7 dB	1.28%	6.36 GHz	10.3 dB	2.03%
A5	7.88 GHz	19.1 dB	0.86%	7.93 GHz	11.6 dB	1.39%
S6	9.49 GHz	18.4 dB	1.41%	9.56 GHz	12.8 dB	2.15%
A7	10.6 GHz	26.5 dB	0.80%	10.63 GHz	23.5 dB	0.96%
S8	12.0 GHz	25.4 dB	0.81%	12.08 GHz	24.0 dB	1.62%
A9	13.6 GHz	23.3 dB	0.47%	13.58 GHz	25.2 dB	0.55%
S10	15.1 GHz	37.9 dB	0.41%	15.15 GHz	27.8 dB	0.82%

* Average IL for the matched case to mitigate the effects of multi-reflections

S10 between 4.46 GHz and 15.1 GHz. An IL of 19.7 dB and a 3-dB FBW of 5.08% are obtained for S2 at 4.41 GHz. An IL of 15.7 dB and a 3-dB FBW of 1.28% are obtained for S4 at 6.32 GHz. The key parameters for other bands are listed in Table VII. Compared to the simulation in Fig. 10 (a), three major differences can be found. First, an increase in IL, especially for the higher frequency bands, is observed, because of the existence of the PL. It also implies that the PL is higher for higher-order modes, agreeing with the observation of COBAR in Section V-A. Second, larger RL is seen at a higher frequency caused by the electrical loading of IDTs [47]. Third, f_c of the higher-order Lamb waves are lower in the measurement because the actual film stack [Fig. 13 (c)] is slightly thicker than the designed 1.2 μm, which shifts the dispersion of Lamb waves to lower frequencies. Nevertheless, the COP Z-cut LiNbO$_3$ enables the efficient transduction of higher-order Lamb waves. More importantly, pronounced ADL passband at 15.1 GHz is electrically measured for the first time, showing the potentials of the COP Z-cut LiNbO$_3$ platform as a great high-frequency micro-acoustic testbed.

Next, the measured performance is conjugately matched to 296+j412 Ω based on the S2 band, using Keysight ADS [Fig. 18 (b)]. The average IL and 3-dB FBW are obtained from the smoothed transmission (400-point-window from measured data). An average IL of 7.5 dB and a 3-dB FBW of 7.55% are obtained for S2 at 4.46 GHz. An average IL of 10.3 dB and a 3-dB FBW of 2.03% are obtained for S4 at 6.36 GHz. These values show that the port impedance mismatch is the main source of IL, and COB-ADLs for larger W_a can be designed if a 50 Ω device is desired. The parameters for other modes are shown in Table VII.

COB-ADLs with different L_g (between 20 μm and 1280 μm) are measured for exploring the major propagation parameters (v_g and PL) of the higher-order Lamb waves. IL, RL, and group delay are plotted in Fig. 19 with both ports terminated with 50 Ω. The passbands for Lamb waves of different orders are highlighted. Compared to the simulated results (Fig. 11), the first difference is that devices with different L_g show different IL due to the PL. Second,
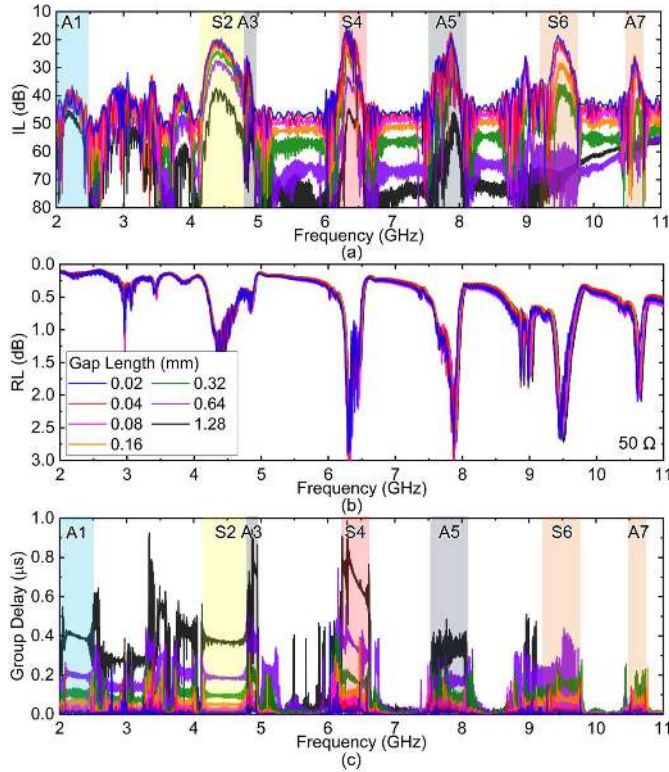
Fig. 19. Measured (a) IL, (b) RL, and (c) group delay of COB-ADLs with different L_g of 20, 40, 80, 160, 320, 640, and 1280 μm, but the same transducer design (Table III).
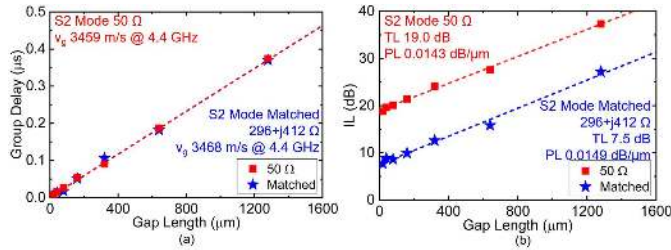

Fig. 20. (a) Group delay and (b) IL of S2 from COB-ADLs with different L_g. v_g, PL, and TL are extracted.

the in-band ripples in IL and group delay are mitigated, because the weak resonances between the transducers are significantly damped. The dispersion of different modes is clearly shown in the group delay measurement.

Based on the COB-ADL platform, the v_g and PL of different modes can be extracted. We first study the group delay [Fig. 20 (a)] and IL [Fig. 20 (b)] of S2 at the center frequency (4.4 GHz) for both the matched and 50 Ω cases. The extracted v_g of S2 is 3.46 km/s, agreeing with the eigenmode FEA obtained value of 3.50 km/s. The extracted PL is 0.0143 dB/μm, which is less than the previously reported PL of A1 ADLs in the conventional Z-cut LiNbO$_3$ (above 0.02 dB/μm [47]). Such significantly reduced PL further validates the advantage of low loss in the COP platform. The transducer loss (TL) is also obtained, showing a TL of 7.5 dB for the matched case, and a TL of 19.0 dB for the 50 Ω case, with the difference caused by the impedance
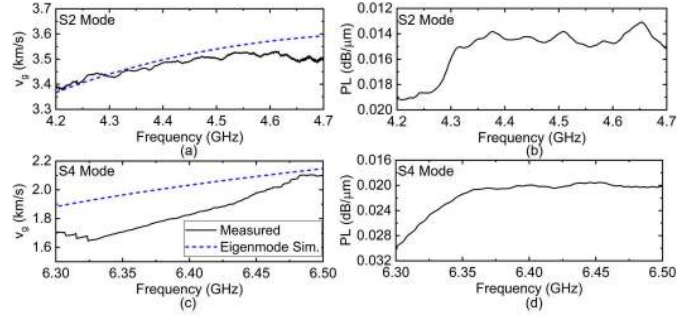

Fig. 21. Extracted v_g and PL of (a) (b) S2 and (c) (d) S4 within the passband. v_g from the eigenmode simulation is also plotted.

TABLE VIII
REPORTED GHz ADL PERFORMANCE WITH SUB-20 dB IL

Ref.	Piezo. Thick.	Feature Size	f_c	IL	FBW	PL
[77]	bulk	0.5 μm	2.1 GHz	18 dB	8.5%	N/A
[78]	bulk	0.4 μm	2.4 GHz	5.5 dB	3.8%	N/A
[69]	0.8 μm	0.8 μm	1.0 GHz	3.7 dB	4.0%	0.001 dB/μm
[79]	0.8 μm	0.45 μm	1.0 GHz	3.2 dB	3.9%	0.005 dB/μm
[80]	1.0 μm	3.0 μm	1.0 GHz	4.9 dB	5.3%	0.003 dB/μm
[47]	0.5 μm	0.6 μm	5.0 GHz	7.9 dB*	4.0%	0.021 dB/μm
[51]	0.5 μm	0.6 μm	8.5 GHz	13.3 dB*	1.2%	0.044 dB/μm
S2	**1.2 μm**	**0.6 μm**	**4.5 GHz**	**7.5 dB***	**7.6%**	**0.014 dB/μm**
S4	**1.2 μm**	**0.6 μm**	**6.4 GHz**	**10.3 dB***	**2.0%**	**0.020 dB/μm**
A5	**1.2 μm**	**0.6 μm**	**7.9 GHz**	**11.6 dB***	**1.4%**	**0.021 dB/μm**
S6	**1.2 μm**	**0.6 μm**	**9.6 GHz**	**12.8 dB***	**2.2%**	**0.057 dB/μm**

* Average IL for the matched case to mitigate the effects of multi-reflections

mismatch. Following the same procedure for extracting the propagation parameters at the center frequency, the v_g and PL within the S2 and S4 passbands are extracted (Fig. 21). v_g around 3.5 km/s for S2 and 1.8 km/s for S4 is obtained. The results agree well with that directly obtained from eigenmode FEA (Section II-C, plotted in Fig. 21), showing a lower v_g at the lower frequencies within each band. The S2 band has a PL around 0.015 dB/μm, while the S4 has a PL approximately 0.020 dB/μm in the passband. The higher PL of Lamb waves with a larger mode order agrees with that obtained in the COBAR case (Fig. 18). The loss mechanisms in COP platforms will be studied in future works. A rigorous extraction requires a set of controlled groups to identify different damping sources, such as loss from the surface, the bonding layer, and the intrinsic acoustic attenuation in LiNbO$_3$. Another interesting aspect of studying is the temperature coefficient of frequency for the COP platform, which will be performed in future works with better-designed test structures [55].

The achieved performance is compared to the prior publications on GHz ADLs with sub-20 dB IL (Table VIII), including SAW ADLs [77], [78], thin-film fundamental plate mode (fundamental symmetric and fundamental shear horizontal)

ADLs [69], [79], [80], and also higher-order Lamb wave ADLs in single-layer structures [47], [51]. The feature sizes and the film thickness are also listed. COB-ADLs maintain the merits of ADLs using higher-order Lamb waves, achieving high f_c with large feature sizes. More importantly, compared to the conventional single-layer higher-order Lamb wave devices, IL and PL of the COP platform have been remarkably reduced, because of the thicker film stack. Note that the IL of the COB-ADLs can be substantially reduced using the unidirectional transducer designs [72]. Upon optimization, S2 COB-ADLs with 3 dB IL at 4.5 GHz can be expected.

To conclude, high-performance COBARs and COB-ADLs have been experimentally measured based on the proposed COP Z-cut LiNbO₃ platform. Their demonstrated high k^2, low attenuation, and high operation frequencies show the great potentials of the platform as a key enabler for 5G NR acoustic solutions.

VI. Conclusion

In this work, the COP Z-cut LiNbO₃ has been demonstrated as a promising platform for higher-order Lamb wave devices with simultaneously low-loss, large k^2, and, most importantly, great frequency scalability. The theoretical framework for COP platforms is derived, showing good agreement with the measurement and can be readily extended to other piezoelectric platforms. Both the resonant devices (COBARs) and non-resonant testbeds (COB-ADLs) have been designed and implemented based on the COP Z-cut LiNbO₃ platform. The fabricated resonator shows an S2 resonance at 3.05 GHz with a high Q of 657, and a large k^2 of 21.5% and an S6 resonance at 9.05 GHz with a high Q of 636 and a k^2 of 3.71%, both among the highest demonstrated for gigahertz higher-order Lamb wave LiNbO₃ devices. The fabricated ADLs show an average IL of 7.5 dB and the lowest reported PL of 0.014 dB/μm at 4.4 GHz for S2. Notable acoustic passbands up to 15.1 GHz are identified. Upon further optimizations, the proposed COP platform can lead to low-loss wideband acoustic components for 5G NR.

Acknowledgment

References

[1] S. Parkvall, E. Dahlman, A. Furuskar, and M. Frenne, "NR: The new 5G radio access technology," *IEEE Commun. Standards Mag.*, vol. 1, no. 4, pp. 24–30, Dec. 2017.

[2] P. Popovski, K. F. Trillingsgaard, O. Simeone, and G. Durisi, "5G wireless network slicing for eMBB, URLLC, and mMTC: A communication-theoretic view," *IEEE Access*, vol. 6, pp. 55765–55779, 2018.

[3] J. Lee *et al.*, "Spectrum for 5G: Global status, challenges, and enabling technologies," *IEEE Commun. Mag.*, vol. 56, no. 3, pp. 12–18, Mar. 2018.

[4] F. Boccardi, R. W. Heath, Jr., A. Lozano, T. L. Marzetta, and P. Popovski, "Five disruptive technology directions for 5G," *IEEE Commun. Mag.*, vol. 52, no. 2, pp. 74–80, Feb. 2014.

[5] L. Laughlin *et al.*, "Emerging hardware enablers for more efficient use of the spectrum," in *Proc. IEEE Int. Symp. Dyn. Spectr. Access Netw. (DySPAN)*, Nov. 2019, pp. 1–9.

[6] K. Hashimoto, *Surface Acoustic Wave Devices in Telecommunications: Modelling and Simulation*. Springer, 2013.

[7] L. A. Coldren and R. L. Rosenberg, "Surface-acoustic-wave resonator filters," *Proc. IEEE*, vol. 67, no. 1, pp. 147–158, Jan. 1979.

[8] A. Hagelauer, G. Fattinger, C. C. W. Ruppel, M. Ueda, K.-Y. Hashimoto, and A. Tag, "Microwave acoustic wave devices: Recent advances on architectures, modeling, materials, and packaging," *IEEE Trans. Microw. Theory Techn.*, vol. 66, no. 10, pp. 4548–4562, Oct. 2018.

[9] R. Ruby, "A snapshot in time: The future in filters for cell phones," *IEEE Microw. Mag.*, vol. 16, no. 7, pp. 46–59, Aug. 2015.

[10] K. Hashimoto, *RF Bulk Acoustic Wave Filters for Communications*. Norwood, MA, USA: Artech House, 2009.

[11] V. Chauhan, C. Huck, A. Frank, W. Akstaller, R. Weigel, and A. Hagelauer, "Enhancing RF bulk acoustic wave devices: Multiphysical modeling and performance," *IEEE Microw. Mag.*, vol. 20, no. 10, pp. 56–70, Oct. 2019.

[12] S. Gong and G. Piazza, "Design and analysis of lithium–niobate-based high electromechanical coupling RF-MEMS resonators for wideband filtering," *IEEE Trans. Microw. Theory Techn.*, vol. 61, no. 1, pp. 403–414, Jan. 2013.

[13] T. Nishihara, T. Yokoyama, T. Miyashita, and Y. Satoh, "High performance and miniature thin film bulk acoustic wave filters for 5 GHz," in *Proc. IEEE Ultrason. Symp.*, Oct. 2002, pp. 969–972.

[14] H. Odagawa and K. Yamanouchi, "10 GHz range extremely low-loss ladder type surface acoustic wave filter," in *Proc. IEEE Ultrason. Symp.*, Oct. 1998, pp. 103–106.

[15] I. L. Bajak, A. McNab, J. Richter, and C. D. W. Wilkinson, "Attenuation of acoustic waves in lithium niobate," *J. Acoust. Soc. Amer.*, vol. 69, no. 3, pp. 689–695, Mar. 1981.

[16] J. Rodriguez *et al.*, "Direct detection of Akhiezer damping in a silicon MEMS resonator," *Sci. Rep.*, vol. 9, no. 1, p. 2244, Dec. 2019.

[17] K. M. Lakin, "Electrode resistance effects in interdigital transducers," *IEEE Trans. Microw. Theory Techn.*, vol. 22, no. 4, pp. 418–424, Apr. 1974.

[18] R. Lu and S. Gong, "Study of thermal nonlinearity in lithium niobate-based MEMS resonators," in *Proc. 18th Int. Solid-State Sens., Actuators Microsyst. Conf. (TRANSDUCERS)*, Jun. 2015, pp. 8–11.

[19] J. Segovia-Fernandez and G. Piazza, "Thermal nonlinearities in contour mode AlN resonators," *J. Microelectromech. Syst.*, vol. 22, no. 4, pp. 976–985, Aug. 2013.

[20] V. Kaajakari, T. Mattila, A. Oja, and H. Seppa, "Nonlinear limits for single-crystal silicon microresonators," *J. Microelectromech. Syst.*, vol. 13, no. 5, pp. 715–724, Oct. 2004.

[21] M. Kadota and S. Tanaka, "Wideband acoustic wave resonators composed of hetero acoustic layer structure," *Jpn. J. Appl. Phys.*, vol. 57, no. 7S1, pp. 7–12, 2018.

[22] M. Kadota, Y. Ishii, T. Shimatsu, M. Uomoto, and S. Tanaka, "Suprious-free, Near-Zero-TCF hetero acoustic layer (HAL)SAW resonators using LiTaO3 thin plate on quartz," in *Proc. IEEE Int. Ultrason. Symp. (IUS)*, Oct. 2018, pp. 1–9.

[23] T. Takai *et al.*, "I.H.P. SAW technology and its application to microacoustic components (Invited)," in *Proc. IEEE Int. Ultrason. Symp. (IUS)*, Sep. 2017, pp. 1–8.

[24] T. Kimura *et al.*, "A high velocity and wideband SAW on a thin LiNbO₃ plate bonded on a Si substrate in the SHF range," in *Proc. IEEE Int. Ultrason. Symp. (IUS)*, Oct. 2019, pp. 1239–1248.

[25] T. Kimura, M. Omura, Y. Kishimoto, and K. Hashimoto, "Comparative study of acoustic wave devices using thin piezoelectric plates in the 3–5-GHz range," *IEEE Trans. Microw. Theory Techn.*, vol. 67, no. 3, pp. 915–921, Mar. 2019.

[26] M. Akiyama, T. Kamohara, K. Kano, A. Teshigahara, Y. Takeuchi, and N. Kawahara, "Enhancement of piezoelectric response in scandium aluminum nitride alloy thin films prepared by dual reactive cosputtering," *Adv. Mater.*, vol. 21, no. 5, pp. 593–596, Feb. 2009.

[27] M. Bousquet *et al.*, "Single-mode high frequency LiNbO3 film bulk acoustic resonator," in *Proc. IEEE Int. Ultrason. Symp. (IUS)*, Oct. 2019, pp. 84–87.

[28] T. Yokoyama, Y. Iwazaki, Y. Onda, T. Nishihara, Y. Sasajima, and M. Ueda, "Highly piezoelectric co-doped AlN thin films for wideband FBAR applications," *IEEE Trans. Ultrason., Ferroelectr., Freq. Control*, vol. 62, no. 6, pp. 1007–1015, Jun. 2015.

[29] Y. Shen, P. Patel, R. Vetury, and J. B. Shealy, "452 MHz bandwidth, high rejection 5.6 GHz UNII XBAW coexistence filters using doped AlN-on-silicon," in *IEDM Tech. Dig.*, Dec. 2019, pp. 17.6.1–17.6.4.

[30] L. Colombo, A. Kochhar, C. Xu, G. Piazza, S. Mishin, and Y. Oshmyansky, "Investigation of 20% scandium-doped aluminum nitride films for MEMS laterally vibrating resonators," in *Proc. IEEE Int. Ultrason. Symp. (IUS)*, Sep. 2017, pp. 1–4.

[31] M. Park, Z. Hao, D. G. Kim, A. Clark, R. Dargis, and A. Ansari, "A 10 GHz single-crystalline scandium-doped aluminum nitride lamb-wave resonator," in *Proc. 20th Int. Conf. Solid-State Sens., Actuators Microsyst. Eurosensors XXXIII (TRANSDUCERS EUROSENSORS XXXIII)*, Jun. 2019, pp. 450–453.

[32] C. Cassella, Y. Hui, Z. Qian, G. Hummel, and M. Rinaldi, "Aluminum nitride cross-sectional Lamé mode resonators," *J. Microelectromech. Syst.*, vol. 25, no. 2, pp. 275–285, Apr. 2016.

[33] A. Bogner *et al.*, "Impact of high sc content on crystal morphology and RF performance of sputtered $Al_{1-x}Sc_xN$ SMR BAW," in *Proc. IEEE Int. Ultrason. Symp. (IUS)*, Oct. 2019, pp. 706–709.

[34] C. Zuo, C. He, W. Cheng, and Z. Wang, "Hybrid filter design for 5G using IPD and acoustic technologies," in *Proc. IEEE Int. Ultrason. Symp. (IUS)*, Oct. 2019, pp. 269–272.

[35] D. Psychogiou, R. Gomez-Garcia, R. Loeches-Sanchez, and D. Peroulis, "Hybrid acoustic-wave-lumped-element resonators (AWLRs) for high-Q bandpass filters with quasi-elliptic frequency response," *IEEE Trans. Microw. Theory Techn.*, vol. 63, no. 7, pp. 2233–2244, Jul. 2015.

[36] X. Lu, K. Mouthaan, and Y. T. Soon, "Wideband bandpass filters with SAW-filter-like selectivity using chip SAW resonators," *IEEE Trans. Microw. Theory Techn.*, vol. 62, no. 1, pp. 28–36, Jan. 2014.

[37] M. Wagner, T. Gossmann, J. Tomasik, R. Weigel, and A. Hagelauer, "Investigations of a new design concept for wide-band hybrid ladder filters," in *Proc. IEEE Int. Ultrason. Symp. (IUS)*, Oct. 2019, pp. 2564–2567.

[38] M. Kadota, T. Ogami, K. Yamamoto, H. Tochishita, and Y. Negoro, "High-frequency Lamb wave device composed of MEMS structure using $LiNbO_3$ thin film and air gap," *IEEE Trans. Ultrason., Ferroelectr., Freq. Control*, vol. 57, no. 11, pp. 2564–2571, Nov. 2010.

[39] Y. Yang, A. Gao, R. Lu, and S. Gong, "5 GHz lithium niobate MEMS resonators with high FoM of 153," in *Proc. IEEE 30th Int. Conf. Micro Electro Mech. Syst. (MEMS)*, Jan. 2017, pp. 942–945.

[40] V. Plessky, S. Yandrapalli, P. J. Turner, L. G. Villanueva, J. Koskela, and R. B. Hammond, "5 GHz laterally-excited bulk-wave resonators (XBARs) based on thin platelets of lithium niobate," *Electron. Lett.*, vol. 55, no. 2, pp. 98–100, Jan. 2019.

[41] N. Assila, M. Kadota, and S. Tanaka, "High-frequency resonator using A1 Lamb wave mode in $LiTaO_3$ plate," *IEEE Trans. Ultrason., Ferroelectr., Freq. Control*, vol. 66, no. 9, pp. 1529–1535, Sep. 2019.

[42] R. S. Weis and T. K. Gaylord, "Lithium niobate: Summary of physical properties and crystal structure," *Appl. Phys. A, Solids Surf.*, vol. 37, no. 4, pp. 191–203, Aug. 1985.

[43] R. T. Schermer and T. H. Stievater, "Millimeter-wave dielectric properties of highly refractive single crystals characterized by waveguide cavity resonance," *IEEE Trans. Microw. Theory Techn.*, vol. 67, no. 3, pp. 1078–1087, Mar. 2019.

[44] Y. Yang, R. Lu, L. Gao, and S. Gong, "4.5 GHz lithium niobate MEMS filters with 10% fractional bandwidth for 5G front-ends," *J. Microelectromech. Syst.*, vol. 28, no. 4, pp. 575–577, Aug. 2019.

[45] P. J. Turner *et al.*, "5 GHz band n79 wideband microacoustic filter using thin lithium niobate membrane," *Electron. Lett.*, vol. 55, no. 17, pp. 942–944, Aug. 2019.

[46] Y. Yang, R. Lu, L. Gao, and S. Gong, "A C-band lithium Niobate MEMS Filter with 10% fractional bandwidth for 5G front-ends," in *Proc. IEEE Int. Ultrason. Symp.*, Oct. 2019, pp. 1981–1984.

[47] R. Lu, Y. Yang, M.-H. Li, M. Breen, and S. Gong, "5-GHz antisymmetric mode acoustic delay lines in lithium niobate thin film," *IEEE Trans. Microw. Theory Techn.*, vol. 68, no. 2, pp. 573–589, Feb. 2020.

[48] Y. Yang, R. Lu, and S. Gong, "A 1.65 GHz lithium niobate A1 resonator with electromechanical coupling of 11.4% and Q of 3112," in *Proc. IEEE Int. Conf. Micro Electro Mech. Syst.*, Jan. 2019, pp. 875–878.

[49] Y. Yang, R. Lu, and S. Gong, "Scaling acoustic filters towards 5G," in *IEDM Tech. Dig.*, Dec. 2018, pp. 36–39.

[50] Y. Yang, R. Lu, T. Manzaneque, and S. Gong, "Toward Ka band acoustics: Lithium niobate asymmetrical mode piezoelectric MEMS resonators," in *Proc. IEEE Int. Freq. Control Symp. (IFCS)*, May 2018, pp. 1–5.

[51] R. Lu, Y. Yang, M. Breen, M.-H. Li, and S. Gong, "8.5 GHz and 11.5 GHz acoustic delay lines using higher-order Lamb modes in lithium niobate thin film," in *Proc. IEEE 33rd Int. Conf. Micro Electro Mech. Syst. (MEMS)*, Jan. 2020, pp. 1242–1245.

[52] K. Nakamura, H. Ando, and H. Shimizu, "Partial domain inversion in $LiNbO_3$ plates and its applications to piezoelectric devices," in *Proc. IEEE Ultrason. Symp.*, Nov. 1986, pp. 719–722.

[53] K. Nakamura and H. Shimizu, "Local domain inversion in ferroelectric crystals and its application to piezoelectric devices," in *Proc. IEEE Ultrason. Symp.*, Oct. 1989, pp. 309–318.

[54] A. Tourlog, K. Nakamura, and H. Shimizu, "SH-type leaky surface waves on rotated Y-cut $LiTaO_3$ substrates with a ferroelectric inversion layer," *Jpn. J. Appl. Phys.*, vol. 30, no. S1, p. 159, Jan. 1991.

[55] K. Nakamura and A. Tourlog, "Effect of a ferroelectric inversion layer on the temperature characteristics of SH-type surface acoustic waves on $36°$ Y-X $LiTaO_3$ substrates," *IEEE Trans. Ultrason., Ferroelectr., Freq. Control*, vol. 41, no. 6, pp. 872–875, Nov. 1994.

[56] D. H. Cortes, S. K. Datta, and O. M. Mukdadi, "Dispersion of elastic guided waves in piezoelectric infinite plates with inversion layers," *Int. J. Solids Struct.*, vol. 45, nos. 18–19, pp. 5088–5102, Sep. 2008.

[57] D. H. Cortes, S. K. Datta, and O. M. Mukdadi, "Elastic guided wave propagation in a periodic array of multi-layered piezoelectric plates with finite cross-sections," *Ultrasonics*, vol. 50, no. 3, pp. 347–356, Mar. 2010.

[58] B. A. Auld, *Acoustic Fields and Waves in Solids*. Melbourne, FL, USA: Krieger, 1990.

[59] I. E. Kuznetsova, B. D. Zaitsev, S. G. Joshi, and I. A. Borodina, "Investigation of acoustic waves in thin plates of lithium niobate and lithium tantalate," *IEEE Trans. Ultrason., Ferroelectr., Freq. Control*, vol. 48, no. 1, pp. 322–328, Jan. 2001.

[60] R. Wang, S. A. Bhave, and K. Bhattacharjee, "Low TCF lithium tantalate contour mode resonators," in *Proc. IEEE Int. Freq. Control Symp. (FCS)*, May 2014, pp. 1–4.

[61] M. Kadota, Y. Ishii, and S. Tanaka, "Ultra-wideband T- and π-type ladder filters using a fundamental shear horizontal mode plate wave in a $LiNbO_3$ plate," *Jpn. J. Appl. Phys.*, vol. 58, no. SG, Jul. 2019, Art. no. SGGC10.

[62] A. Kochhar, G. Vidal-Alvarez, L. Colombo, and G. Piazza, "Top electrode shaping for harnessing high coupling in thickness shear mode resonators in Y-cut lithium niobate thin films," in *Proc. IEEE Micro Electro Mech. Syst. (MEMS)*, Jan. 2018, pp. 71–74.

[63] S. H. Chang, N. N. Rogacheva, and C. C. Chou, "Analysis of methods for determining electromechanical coupling coefficients of piezoelectric elements," *IEEE Trans. Ultrason., Ferroelectr., Freq. Control*, vol. 42, no. 4, pp. 630–640, Jul. 1995.

[64] T. Yanagitani, K. Arakawa, K. Kano, A. Teshigahara, and M. Akiyama, "Giant shear mode electromechanical coupling coefficient k_{15} in C-axis tilted ScAlN films," in *Proc. IEEE Int. Ultrason. Symp.*, Oct. 2010, pp. 2095–2098.

[65] R. Karasawa and T. Yanagitani, "C-axis Zig-Zag polarization inverted ScAlN multilayer for FBAR transformer rectifying antenna," in *Proc. IEEE Int. Ultrason. Symp. (IUS)*, Sep. 2017, pp. 1–4.

[66] T. Yanagitani, N. Morisato, S. Takayanagi, M. Matsukawa, and Y. Watanabe, "C-axis Zig-Zag ZnO film ultrasonic transducers for designing longitudinal and shear wave resonant frequencies and modes," *IEEE Trans. Ultrason., Ferroelectr., Freq. Control*, vol. 58, no. 5, pp. 1062–1068, May 2011.

[67] M. Levy *et al.*, "Fabrication of single-crystal lithium niobate films by crystal ion slicing," *Appl. Phys. Lett.*, vol. 73, no. 16, pp. 2293–2295, Oct. 1998.

[68] F. I. Fedorov, *Theory of Elastic Waves in Crystals*. Springer, 2013.

[69] R. Lu, T. Manzaneque, Y. Yang, M.-H. Li, and S. Gong, "Gigahertz low-loss and wideband S0 mode lithium niobate acoustic delay lines," *IEEE Trans. Ultrason., Ferroelectr., Freq. Control*, vol. 66, no. 8, pp. 1373–1386, Aug. 2019.

[70] *IEEE Standard on Piezoelectricity*, ANSI/IEEE Standard 176-1987, 1988.

[71] R. Lu, M.-H. Li, Y. Yang, T. Manzaneque, and S. Gong, "Accurate extraction of large electromechanical coupling in piezoelectric MEMS resonators," *J. Microelectromech. Syst.*, vol. 28, no. 2, pp. 209–218, Apr. 2019.

[72] C. S. Hartmann and B. P. Abbott, "Overview of design challenges for single phase unidirectional SAW filters," in *Proc. IEEE Ultrason. Symp.*, Oct. 1989, pp. 79–89.

[73] T. Manzaneque, R. Lu, Y. Yang, and S. Gong, "Low-loss and wideband acoustic delay lines," *IEEE Trans. Microw. Theory Techn.*, vol. 67, no. 4, pp. 1379–1391, Apr. 2019.

[74] T. Manzaneque, R. Lu, Y. Yang, and S. Gong, "Lithium niobate MEMS chirp compressors for near zero power wake-up radios," *J. Microelectromech. Syst.*, vol. 26, pp. 1204–1215, Sep. 2017.

[75] J. D. Larson, P. D. Bradley, S. Wartenberg, and R. C. Ruby, "Modified Butterworth-Van Dyke circuit for FBAR resonators and automated measurement system," in *Proc. IEEE Ultrason. Symp. Int. Symp.*, vol. 1, Oct. 2000, pp. 863–868.

[76] D. A. Feld, R. Parker, R. Ruby, P. Bradley, and S. Dong, "After 60 years: A new formula for computing quality factor is warranted," in *Proc. IEEE Ultrason. Symp.*, Nov. 2008, pp. 431–436.

[77] C.-Y. Jian and S. Beaudin, "A new type SPUDT SAW for use in high frequency around 2 GHz," in *Proc. IEEE Ultrason. Symp.*, Oct. 2002, pp. 279–282.

[78] S. Lehtonen, V. P. Plessky, C. S. Hartmann, and M. M. Salomaa, "SPUDT filters for the 2.45 GHz ISM band," *IEEE Trans. Ultrason., Ferroelectr., Freq. Control*, vol. 51, no. 12, pp. 1697–1703, Dec. 2004.

[79] R. Lu, Y. Yang, M.-H. Li, T. Manzaneque, and S. Gong, "GHz broadband SH0 mode lithium niobate acoustic delay lines," *IEEE Trans. Ultrason., Ferroelectr., Freq. Control*, vol. 67, no. 2, pp. 402–412, Feb. 2020.

[80] R. Lu, S. Link, and S. Gong, "A unidirectional transducer design for scaling GHz AlN-based RF microsystems," *IEEE Trans. Ultrason., Ferroelectr., Freq. Control*, vol. 67, no. 6, pp. 1250–1257, Jun. 2020.

Yansong Yang (Member, IEEE) received the B.S. degree in electrical and electronic engineering from the Huazhong University of Science and Technology, Wuhan, China, in 2014, and the M.S. and Ph.D. degrees in electrical engineering from the University of Illinois at Urbana–Champaign (UIUC), Urbana, IL, USA, in 2017 and 2019, respectively. He is currently a Post-Doctoral Researcher with UIUC. His research interests include the design and microfabrication techniques of RF MEMS resonators, filters, switches, and photonic integrated circuits. He received the Second Place in the Best Paper Competition at the 2018 IEEE International Microwave Symposium and the Best Paper Award at the 2019 IEEE International Ultrasonics Symposium. He was also a Finalist for the Best Paper Award at the 2018 IEEE International Frequency Control Symposium. He was also a recipient of the 2019 P. D. Coleman Graduate Research Award from the Department of Electrical and Computer Engineering, UIUC.
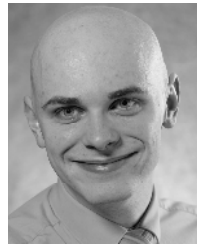
Steffen Link (Student Member, IEEE) received the B.S. degree in computer engineering from the South Dakota School of Mines and Technology, Rapid City, South Dakota. He is currently pursuing the master's degree with the University of Illinois at Urbana–Champaign, IL, USA. His research interest includes the design and microfabrication techniques of MEMS resonators, filters, and other radio frequency microsystems.
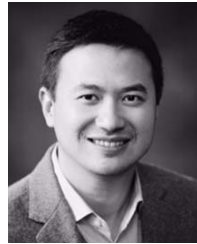
Songbin Gong (Senior Member, IEEE) received the Ph.D. degree in electrical engineering from the University of Virginia, Charlottesville, VA, USA, in 2010. He is currently an Associate Professor and the Intel Alumni Fellow with the Department of Electrical and Computer Engineering and the Micro and Nanotechnology Laboratory, University of Illinois at Urbana–Champaign, Urbana, IL, USA. His primary research interest includes the design and implementation of radio frequency microsystems, components, and subsystems for reconfigurable RF front ends. In addition, his research interest includes hybrid microsystems based on the integration of MEMS devices with photonics or circuits for signal processing and sensing. He is a Technical Committee Member of MTT-21 RF-MEMS of the IEEE Microwave Theory and Techniques Society, the International Frequency Control Symposium, and the International Electron Devices Meeting. He was a recipient of the 2014 Defense Advanced Research Projects Agency Young Faculty Award, the 2017 NASA Early Career Faculty Award, the 2019 UIUC College of Engineer Dean's Award for Excellence in Research, and the 2019 Ultrasonics Early Career Investigator Award. Along with his students and post-doctoral researchers, he received the Best Paper Awards from the 2017 and 2019 IEEE International Frequency Control Symposium and the 2018 and 2019 International Ultrasonics Symposium and received the Second Place in the Best Paper Competition at the 2018 IEEE International Microwave Symposium. He currently serves as the Chair for MTT TC2 and TC 21 and an Associate Editor for the IEEE TRANSACTIONS ON ULTRASONICS, FERROELECTRICS, AND FREQUENCY CONTROL (TUFFC) and the JOURNAL OF MICRELECTROMECHANICAL SYSTEMS (JMEMS).

Ruochen Lu (Member, IEEE) received the B.E. degree (Hons.) in microelectronics from Tsinghua University, Beijing, China, in 2014, and the M.S. and Ph.D. degrees in electrical engineering from the University of Illinois at Urbana–Champaign (UIUC), Urbana, IL, USA, in 2017 and 2019, respectively. He is currently a Post-Doctoral Researcher with UIUC. His research interests include radio frequency microsystems and their applications for timing and signal processing. He received the Best Student Paper Awards at the 2017 IEEE International Frequency Control Symposium and the 2018 IEEE International Ultrasonics Symposium. He was also a recipient of the 2015 Lam Graduate Award, the 2017 Nick Holonyak, Jr., Graduate Research Award, the 2018 Nick Holonyak, Jr., Fellowship, and the 2019 Raj Mittra Outstanding Research Award from the Department of Electrical and Computer Engineering, UIUC. He will join the Department of Electrical and Computer Engineering, The University of Texas at Austin, as an Assistant Professor, in January 2021.